Geochemistry, Geophysics, Geosystems®

RESEARCH ARTICLE
10.1029/2024GC012080

Special Collection:
A fresh look at the Caribbean plate geosystems

Demise of the Barra Honda Carbonate Shoal (Costa Rica) at the Paleocene-Eocene Boundary Linked to Climate Change and Forearc Tectonics

Goran Andjić[1], Claudia Baumgartner-Mora[1], Peter O. Baumgartner[1], Maria Rose Petrizzo[2], Torsten Vennemann[3], André N. Paul[4,5], and Valentin Lorenzo[1]

[1]Institute of Earth Sciences, University of Lausanne, Lausanne, Switzerland, [2]Dipartimento di Scienze della Terra, Università degli Studi di Milano, Milano, Italy, [3]Institute of Earth Surface Dynamics, University of Lausanne, Lausanne, Switzerland, [4]Department of Earth Sciences, Section of Earth and Environmental Sciences, University of Geneva, Geneva, Switzerland, [5]Institute of Geosciences, Goethe University Frankfurt, Frankfurt, Germany

Abstract The latest Cretaceous(?)–Paleocene Barra Honda Formation represents one of the largest carbonate shoals (>900 km^2, 350 m thick) of the convergent margin of Costa Rica. Although the mode of formation of the carbonate shoal is well understood, how environmental and tectonic factors interacted to cause its demise near the Paleocene-Eocene boundary remains poorly constrained. Stable isotopic, biostratigraphic, mineralogical, and geochronological analyses from the Barra Honda Formation and overlying siliceous Buenavista Formation provide new constraints on the timing and causes of the demise of the carbonate shoal. We report one new U–Pb zircon chemical abrasion, isotope dilution, and thermal ionization mass spectrometry date (56.30 ± 0.13 Ma, 2σ) obtained from an ash-rich layer at the boundary between the two formations. The sharp transition from Barra Honda massive limestones to Buenavista marl-chert alternations coincides with a negative shift in carbon isotope ($\delta^{13}C_{carb}$) values of about 3–5 ‰ and a 50% decrease in carbonate contents. The timing of the combined lithological-mineralogical-isotopic change is coeval with the Paleocene-Eocene Thermal Maximum (PETM, 56 Ma). The onset of clay-rich sedimentation is consistent with a PETM-related increase in the terrestrial influx of nutrients and detrital particles, which promoted eutrophication and decreased light availability in the photic zone. Combined with seawater acidification and warming, these environmental parameters were fatal to the carbonate-producing benthic communities of Barra Honda. High subsidence rates of the forearc basin and renewed arc volcanic activity must have closely followed the cessation of shallow carbonate production, preventing further formation of the carbonate shoal.

Plain Language Summary The Barra Honda Formation in Costa Rica is a large area of carbonate rocks formed during the latest Cretaceous(?)–Paleocene interval. We wanted to understand why this carbonate shoal, which was formed by a favorable combination of environmental and tectonic factors, disappeared around the Paleocene–Eocene boundary. We studied different aspects, that is, stable isotopes, microfossils, minerals, and ages of rocks from the Barra Honda Formation and the overlying Buenavista Formation. We present a new age date from zircons recovered from an ash layer between these formations, showing that the lithological change happened around 56 million years ago. At that time, there was a sudden shift in the types of sedimentary rocks deposited and in their carbon isotope values. This change coincides with a global event called the Paleocene–Eocene Thermal Maximum (PETM), known for causing environmental upheavals such as ocean warming and increased ocean water acidity. These factors caused more nutrients to flow in from land and reduced light in the seawater, and likely led to the decline of benthic communities in the Barra Honda carbonate shoal. Additionally, the basin where these carbonate rocks formed started sinking rapidly after the PETM event, preventing the shoal from recovering.

Key Points:

- U-Pb age, biostratigraphic, and stable isotope compositions show that the Barra Honda carbonate shoal ended at the Paleocene-Eocene boundary
- PETM-related ocean acidification and increased detrital/nutrient influx may be the primary causes of the demise
- High subsidence rates of the forearc basin during the early Eocene terminated the shallow carbonate sedimentation

Supporting Information:

Supporting Information may be found in the online version of this article.

Correspondence to:

G. Andjić,
goran.andjic@unil.ch

Citation:

Andjić, G., Baumgartner-Mora, C., Baumgartner, P. O., Petrizzo, M. R., Vennemann, T., Paul, A. N., & Lorenzo, V. (2025). Demise of the Barra Honda carbonate shoal (Costa Rica) at the Paleocene-Eocene boundary linked to climate change and forearc tectonics. *Geochemistry, Geophysics, Geosystems*, *26*, e2024GC012080. https://doi.org/10.1029/2024GC012080

Received 27 NOV 2024
Accepted 19 APR 2025

1. Introduction

Shallow-water carbonate production on long-lived (10–60 Ma) large carbonate shelves set along passive margins is thought to be controlled primarily by paleoclimate and eustatic sea level change over short time scales (<1 Ma, e.g., Kemp & Sadler, 2014). In contrast, carbonate production along convergent margins is expected to be primarily controlled by tectonic and volcanic processes over short time scales (e.g., Taylor et al., 2005; Wilson & Lokier, 2002). Hence, the development of chlorozoan carbonates in convergent margins is limited by two key factors (Dorobek, 2008): (a) High inputs of fine-to coarse-grained volcano-detrital particles, produced by tropical

weathering of emerged oceanic terranes, volcanic edifices, and airborne ashes from active volcanoes, can overwhelm carbonate production; (b) the scarcity of sufficiently large photic zones restricts significant carbonate accumulation. When these limiting factors are overcome, shallow-water carbonates may occur (e.g., Bosence, 2005) and are characterized by: (a) Sudden appearance and disappearance of conditions for chlorozoan carbonate production; (b) modest size (1–100 km wide); and (c) a geologically short period (1–10 Ma). These "punctuated chlorozoan carbonates" (Baumgartner-Mora et al., 2019) formed all along the Mid-American convergent margin and consisted of short-lived carbonate banks and buildups, interstratified in generally deep-water turbiditic fore- and back-arc series.

The uppermost Cretaceous (?)–Paleocene Barra Honda Formation (Fm.) of Costa Rica (Dengo, 1962; Figure 1b), largely built of chloralgal carbonate mud, is a good example of a short-lived, moderately sized (originally > 900 km^2) chlorozoan carbonate shoal formed between long-lived episodes of deep-water volcaniclastic sedimentation. The birth and growth of the Barra Honda carbonate shoal has been previously discussed as a biotic response to reduced detrital input and km-scale uplift of a proximal forearc basin (Andjić, Baumgartner, & Baumgartner-Mora, 2018; Baumgartner-Mora & Baumgartner, 2016; Jaccard et al., 2001). In contrast, the disappearance of the Barra Honda shoal has received much less attention. Because it occurred near the Paleocene–Eocene boundary, the demise of the Barra Honda shoal may not be solely attributed to local factors (e.g., forearc tectonics and/or volcaniclastic input) and calls for an examination of a possible causal link with the Paleocene-Eocene Thermal Maximum (PETM).

The abrupt shift from carbonate-rich to carbonate-poor layers–such as the Barra Honda Fm–Buenavista Fm. Boundary–has been described in marine PETM sections around the world. Centimeter-to meter-sized clay-rich layers coincide with the onset of the PETM, with examples from onshore sections (Aubry et al., 2007; Bralower et al., 2018; Giusberti et al., 2007; Schmitz et al., 2001) and offshore drillholes (Borneman et al., 2014; Colosimo et al., 2006; Lyle et al., 2002; Penman, 2016; Wade et al., 2020; Zachos et al., 2004). The interruption of carbonate-rich sedimentation in deep seas has been interpreted as the result of ocean acidification that accompanied the rapid release of large amounts of CO_2 (e.g., Babila et al., 2018; Dickens et al., 1997; Penman et al., 2014; Zachos et al., 2005; Zeebe & Zachos, 2007). The decrease or absence of carbonate accumulation and preservation in deep-water settings was primarily associated with the shallowing of the lysocline and carbonate compensation depth (Gibbs et al., 2010; Murphy et al., 2010; Zachos et al., 2005).

In this study, we combine carbon stable isotope stratigraphy, bulk mineralogy analysis, zircon dating, and micropaleontology to test whether the sudden demise of the Barra Honda Fm. near the Paleocene–Eocene boundary may be primarily controlled by climate change during the PETM. The shallow-water, tectonically active, arc-proximal setting of the Barra Honda carbonate shoal requires a discussion on the interplay of local and global (e.g., ocean acidification) factors in its demise at the Paleocene–Eocene boundary. Understanding how carbonate shoals respond to climatic and tectonic perturbations is crucial, as they serve as stepping stones for the migration of shallow-water benthic communities. Overall, we aim to assess whether short-lived carbonate shoals are capable of recording global climatic events.

2. The Barra Honda Formation

The Barra Honda carbonate shoal crops out in the Tempisque and Nicoya areas as erosional remnants in karstified hills corresponding to anticlines, covering today less than 60 km^2 (Denyer et al., 2014a), but originally covered a surface of >900 km^2 (Baumgartner-Mora & Baumgartner, 2016; Figure 2a). Mora (1981) described two subunits of the Barra Honda Fm. in the Cerro Barra Honda area: (a) A lower, poorly stratified, massive white limestone composed of algal boundstones and some peloid wackestones, largely composed of micrite, and (b) an upper stratified unit of peloidal packstones and oolitic grainstones. Geological mapping (Flores et al., 2003a, 2003b; Jaccard et al., 2001; Rivier, 1983; compilation by Denyer et al., 2014b) shows that the formation rests unconformably on Upper Cretaceous to Paleocene deep-water formations, with a highly diachronous erosional surface (Figure 3) that was subaerial or paralic as suggested in the northernmost outcrops (Cerro Espiritu Santo), where bored limestone clasts are set in an altered matrix of Upper Cretaceous Sabana Grande Fm. (Di Marco et al., 1995; Jaccard et al., 2001; Jaccard & Münster, 2001). In the north, transgression/progradation of the upper Barra Honda over the altered Upper Cretaceous surface starts with lenses of cross-laminated oolitic packstones and grainstones containing *Neodiscocyclina grimsdalei*, thick-shelled *Ranikothalia catenula antillea* and *R. c. tobleri*, as well as large melobesian rhodoids encrusted by *Polystrata alba*, forming bafflestones. These rather high energy, near-

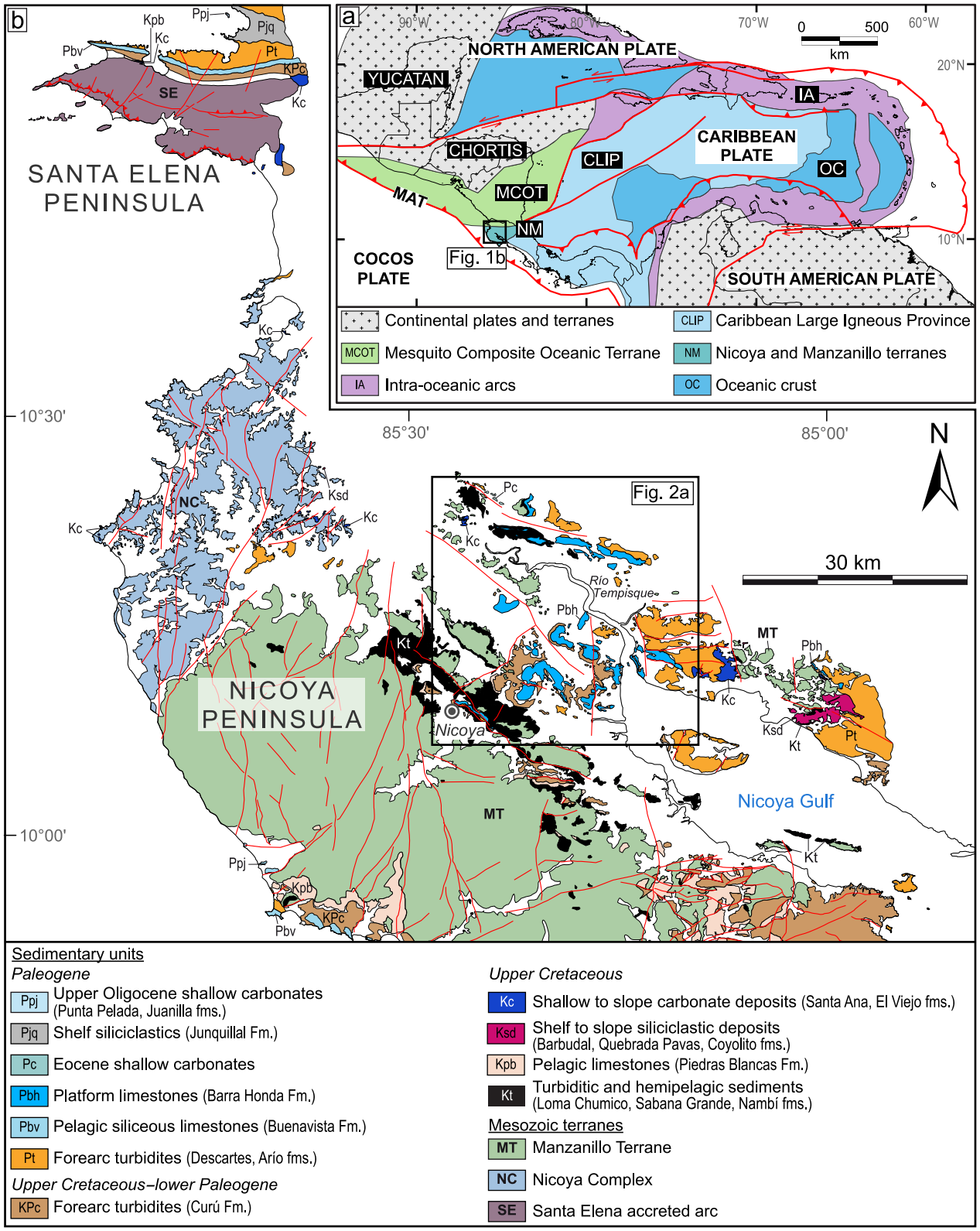

Figure 1. (a) Plate tectonic map illustrating the main units of the Caribbean Plate (modified after Andjić, Escuder-Viruete, et al., 2019; Baumgartner et al., 2008; Escalona et al., 2021; Romito & Mann, 2020; Sanchez et al., 2019). MAT, Middle America Trench. (b) Geological map of northwestern Costa Rica, centered on the Nicoya Peninsula (modified after Andjić et al., 2016, 2018a, 2019a; Baumgartner et al., 1984; Bandini et al., 2008; Denyer et al., 2014b; Denyer & Alvarado, 2007; Escuder-Viruete et al., 2015; Flores et al., 2003a, 2003b; Flores, 2006, 2009; Mora & Baumgartner, 1985; Weber, 2013).

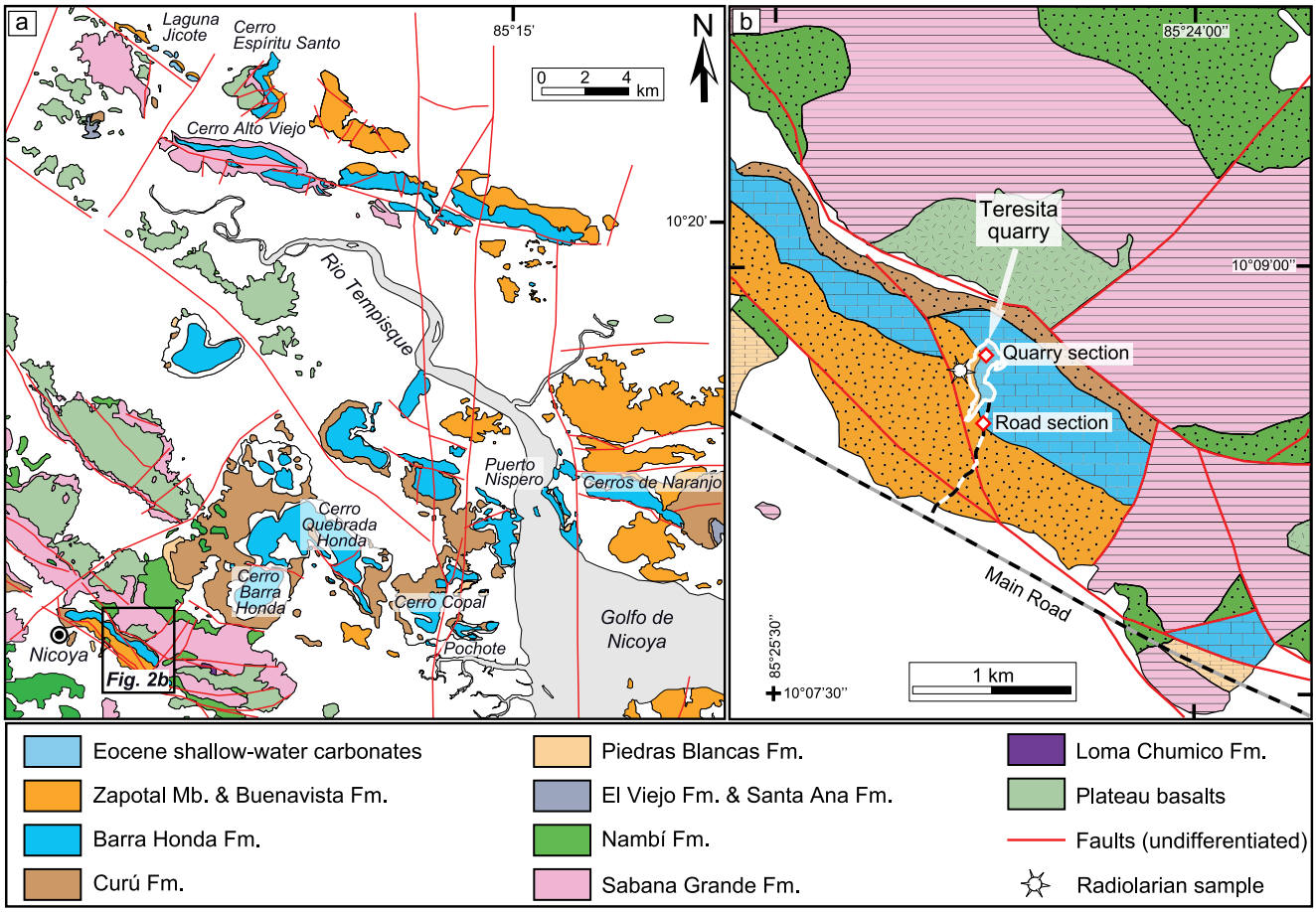

Figure 2. (a) Detailed geological map of the inner Tempisque Forearc Basin showing the outcrops of the Barra Honda Formation (in blue; modified after Baumgartner-Mora & Baumgartner, 2016; Denyer et al., 2014b; Flores et al., 2003a, 2003b). (b) Geological map of the Nicoya town area (modified after Denyer et al., 2014b). The studied road and quarry sections of the upper Barra Honda Formation are indicated.

shore facies are overlain by calm-water neritic wackestones rich in *Distichoplax biserialis*, and thin-shelled *Ranikothalia*, such as *R. catenula catenula* and *R. c. soldadensis* attesting for a late Paleocene age (Baumgartner-Mora & Baumgartner, 2016). Based on the presence of *Ranikothalia*, Calvo and Bolz (1991) established a late Paleocene–early Eocene age of the Espiritu Santo limestones (Figure 2a).

In Pochote (Figures 2a) and Jaccard et al., 2001 described a sequence with abundant reworked pelagic limestone clasts, certainly reworked from the Upper Cretaceous Piedras Blancas Fm. (Figure 3) according to the presence of the late Campanian–Maastrichtian *Globotruncana ventricosa*, included in an open-marine micritic matrix containing the upper Paleocene *Morozovella velascoensis* and *Pseudohastigerina* sp. In the lower part of the Pochote section, Upper Cretaceous lithoclasts were reworked from the substrate cropping up-slope, while intraformational poorly lithified shallow-water clasts dominate in the upper part of the section. Here, the Barra Honda Fm. encroaches with a sharp, but apparently conformable contact over the sandy forearc turbidites of the Paleocene Curú Fm. Up-section, the abundance of shallow-water clasts increases and a typical, massive Barra Honda facies with abundant squamariacean *Polystrata alba* follow toward the top. At Pochote, the onset of Barra Honda Fm. took place in an offshore marine foreslope paleoenvironment without a major erosional hiatus at its base.

Aguilar and Denyer (2001) reported coral patch reefs (CPR) from the eastern outcrops of Barra Honda Fm. near Puerto Nispero (Figure 2a). Chesnel et al. (2024) re-examined the Puerto Nispero outcrops and described Barra Honda facies interbedded with a coral patch reef, which they assigned to the Maastrichtian based on the presence of *Nerinea* and the coral genus *Marcelohelia* sp. These carbonates around Puerto Nispero, along the East bank of the lower Tempisque estuary (Figure 2a) were previously mapped as Barra Honda Fm (Denyer et al., 2014b), and

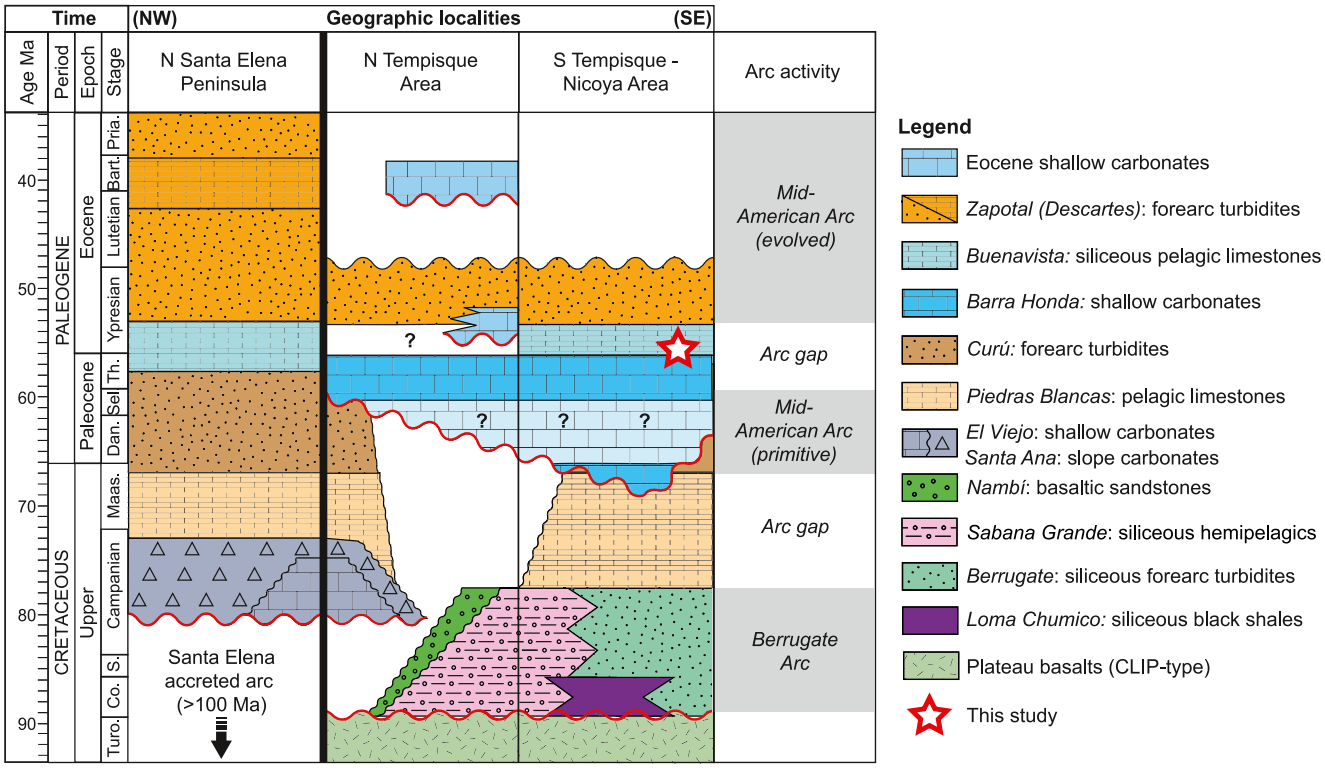

Figure 3. Chronostratigraphic logs of the Tempisque-Nicoya and northern Santa Elena areas (adapted from Baumgartner-Mora and Baumgartner (2016); based on data from Baumgartner et al. (1984), Bandini et al. (2008), Denyer et al. (2014a, 2014b), Andjić et al. (2016, 2018a, 2019a)). Formation names are indicated in italics. Major unconformities are marked with red wavy lines. White areas are stratigraphic gaps due to erosion or non-deposition. Light blue fields with question marks represent temporal uncertainties of stratigraphic gaps. Two successive arc systems are recorded by the forearc sedimentation: the Berrugate Arc, restricted to the Manzanillo Terrane, precedes the docking of the Santa Elena and Nicoya Terranes, while the Mid-American Arc produced forearc sediments in the overlap sequences of the three terranes (see Figure 1b for a terrane map). A temporary arc gap is documented by the Barra Honda carbonate shoal and the overlying pelagic Buenavista Fm.

represent undoubtedly the lowest (and oldest) part of this formation, resting unconformably on hemipelagic lime- and claystone attributed to the Campanian-Maastrichtian Piedras Blancas Fm (Denyer et al., 2014b; Figure 3). Chesnel et al. (2024) defined a new "Puerto Nispero Fm.", which includes both the deformed hemipelagic "claystone" and the unconformably overlying shallow carbonates, defining rather a Maastrichtian "chronozone" than a formation in the sense of the International Code of Stratigraphy (Murphy & Salvador, 1999). However, the illustrated, poorly preserved, planktonic foraminifera of the "claystone" (*Rugoglobigerina rugosa* and *Globotruncanella* sp.) range from middle Campanian to Maastrichtian (Huber et al., 2016; Petrizzo et al., 2020), which fits the age range of the Piedras Blancas Fm.

Baumgartner-Mora and Baumgartner (2016) produced a refined model that shows an asymmetric carbonate shoal fringing an uplifted and tilted area of the forearc. Based on the available biostratigraphic data, these authors postulated a late Paleocene south to north onlap of the Barra Honda shoal. The probably uppermost Cretaceous very shallow coral-bearing Barra Honda facies described by Chesnel et al. (2024) encroached on a local, likely subaerial paleo-high where the substrate was eroded down to the Campanian-Maastrichtian pelagic sediments of the Piedras Blancas Fm. The Puerto Nispero outcrops are located in the core of a roughly North–South-oriented anticline (Denyer et al., 2014b), which is flanked on both sides by higher Barra Honda facies. Although the stratigraphic continuity toward higher Barra Honda facies cannot be observed and fossils attesting for early Paleocene ages are lacking, a stratigraphic continuity can be assumed from lithologic and structural relationships evident in geological maps. Thus, uplift initially took place in the southwest followed by subsidence. This pattern shifted to the northeast, where uplift was again followed by subsidence during the late Paleocene, when a shallow, restricted lagoon produced the chloralgal carbonate mud of the upper Barra Honda Fm. Its high production resulted in sediment export toward deeper offshore areas (e.g., Pochote), where the progradation of the shallow environments finally produced an oolitic rim.

In the hills east of the Nicoya town (Figure 2a), the Barra Honda Fm. rests with a tectonic contact on both the underlying deep-water Curú Fm. and the lower Eocene Zapotal Member (Mb.) of the Descartes Fm (Denyer et al., 2014a, 2014b). The latter was originally mapped as the Upper Cretaceous Sabana Grande Fm. (Flores et al., 2003a), because it contains cherty facies (here considered as part of the pelagic Buenavista Fm.) that resemble those of the deep-water Zapotal Mb. We have modified the geological map (Figure 2b) according to our observations in the Teresita quarry area, and a radiolarian sample described from this unit by Bandini et al. (2008) is reevaluated in this study as early Ypresian (early Eocene) age.

3. Materials and Methods

3.1. Field Work and Sampling

Two upper Paleocene–lower Eocene sections were measured and sampled in the Tajo Santa Teresita (here called "Teresita quarry"), located 4.5 km east of the town of Nicoya (Figure 2b). The quarry section (code TTQ; 10°08′36.66′′N/85°24′47.16′′W) is about 109 m thick, whereas the road section (code TTR; 10°08′24.78′′N/85°24′45.60′′W) is about 3 m thick. The 0-m mark in these stratigraphic logs has been placed at the boundary between the Barra Honda Fm. and the Buenavista Fm.

3.2. Micropaleontological Analysis

Thin sections from 28 samples were examined with an optical microscope to characterize the facies and microfossil content of the Barra Honda Fm., the Buenavista Fm., and the Zapotal Mb. Polished thin sections were scanned with an Olympus VS110 slide scanner. A motor-driven turntable can take several hundred overlapping images to produce an image of about 12'000 × 26'000 pixels with a 4x lens, resulting in a resolution of about 622 pixels/mm (pixel size 1.6 µm). This resolution is sufficient to allow detailed analysis of microfossils across an entire thin section.

For a coherent biochronologic interpretation of new and existing (Text S1 in Supporting Information S1) data on planktonic foraminifera we use the zonation summarized in Olsson et al. (1999), Pearson et al. (2006), Wade et al. (2011), and Huber et al. (2016), and its calibration to absolute time by Speijer et al. (2020), in which the Paleocene–Eocene boundary is defined by the negative $\delta^{13}C$-shift of the PETM (Aubry et al., 2007). For a re-evaluation of a radiolarian assemblage published by Bandini et al. (2008), we use the zonation of Jackett et al. (2008).

3.3. Optical Cathodoluminescence

Forty µm polished thin sections were used for cathodoluminescence optical analyses (CL). CL images were obtained using an OPEA electron gun adapted to the vacuum chamber of a CTTL, Technosyn 8,200 MkII, mounted on an Olympus optical microscope with a mobile tube and an object stage fixed in height. The OPEA was operated at 15–20 kV and 0.4–0.5 mA with an unfocused cold cathode electron beam under an air atmosphere of 0.2 torr.

3.4. CA-ID-TIMS on Zircon

Zircon was separated from the sediment in the laboratories of the University of Lausanne. Approximately 1–2 kg of the ash-rich layer TTR5 was crushed and then decarbonated for 3 days using 35% HCl. After several washings, the sample was treated with hydrogen peroxide (H_2O_2) for 5 days to disperse the clays. The dispersion of the clays was finalized by heating the hydrogen peroxide. The sample was then treated for three weeks with 40% hydrofluoric acid (HF) to dissolve minerals such as quartz or feldspar.

U–Pb chemical abrasion isotope dilution thermal ionization mass spectrometry (CA-ID-TIMS) was used to date the zircon grains at the University of Geneva. Individual zircon crystals free of visible inclusions and cracks were hand-picked using a binocular microscope at a magnification of 20x to 40x. Individual zircons were washed in 3 ml Savillex beakers in an ultrasonic bath 4 times using 7N HNO_3. The zircons were then transferred into individual 200 µL Savillex microcapsules, along with 1–2 drops of HF_{conc} and 1–2 drops of a mixed ^{202}Pb-^{205}Pb-^{233}U-^{235}U tracer solution (ET2535, Condon et al., 2015; McLean et al., 2015), and dissolved at 210°C in a Parr bomb for 48 hr, to ensure complete dissolution. After dissolution, the samples were dried on a hotplate at 120°C, converted to chloride form by addition of 6N HCl and placed back in the Parr bomb over-night.

Finally, the sample was again dried and re-dissolved in 3N HCl, and then U and Pb were separated using a single column anion exchange chemistry. U and Pb were loaded on outgassed, zone-refined, single Re filaments with a silica-gel/phosphoric acid emitter solution (Gerstenberger & Haase, 1997).

Pb was measured in dynamic mode using a Daly detector, while U was measured as an oxide in static mode using Faraday detectors coupled to 1,012 Ω resistor amplifiers. The electronic baselines and amplifier calibration were performed on a weekly basis prior to standard and unknown sample analyses. Measured isotopic ratios were corrected for interferences of $^{238}U^{18}O^{16}O$ on $^{235}U^{16}O_2$ using an $^{18}O/^{16}O$ composition of 0.00205, based on repeated measurements of the U500 standard. Mass fractionation of Pb was calculated and corrected using a $^{202}Pb/^{205}Pb$ ratio of 0.99923913 ± 0.00026555 (1σ) (Condon et al., 2015). For all U analyses, U mass fractionation was corrected using a $^{233}U/^{235}U$ ratio of 0.995062 ± 0.000108 (2σ) and a $^{238}U/^{235}U$ ratio of 137.818 ± 0.045 (2σ) (Condon et al., 2015; Hiess et al., 2012). The common Pb in zircon is considered laboratory blank, and is corrected using the isotopic composition $^{206}Pb/^{204}Pb$ of 17.43 ± 0.71, a $^{207}Pb/^{204}Pb$ of 14.73 ± 0.38 and a $^{208}Pb/^{204}Pb$ of 35.58 ± 1.04. All U-Pb dates are corrected for initial ^{230}Th disequilibrium, assuming a Th/U ratio of the source magma of 3.5 ± 1. During the period of data acquisition, the ET 100 solution was repeatedly analyzed and yielded a weighted mean of 100.176 ± 0.006 Ma (MSWD = 2; n = 22), matching the consensus value of 100.173 ± 0.003 Ma (Schaltegger et al., 2021).

All data were processed using the Tripoli, Redux U-Pb, YourLab and Isoplot software/excel packages (Bowring et al., 2012; Ludwig, 1991; McLean et al., 2011; Schmitz & Schoene, 2007). Weighted mean U-Pb age uncertainties are reported at the 2σ level in the format A ± X/Y/Z, where A is the weighted mean age, X is analytical uncertainty, Y is analytical and tracer uncertainty combined, and Z is analytical, tracer, and decay constant uncertainties combined (Schoene et al., 2006). Lower intercept ages are calculated for samples with assumed inherited components and discordance. The results are presented in Table S1 in Supporting Information S1).

3.5. X-Ray Diffraction on Bulk Rocks

Bulk-rock mineralogy of 29 samples has been analyzed using an X-TRA Thermo-Arl SCINTAG 2000 diffractometer, following the procedures of Kübler (1983) and Adatte et al. (1996). The whole-rock mineralogy was determined by a semi-quantitative method using XRD peak intensities of the main minerals in comparison with external standards (Adatte et al., 1996; Klug & Alexander, 1974; Kübler, 1983). The precision is 5 wt% for grain minerals and 5 to 10 wt% for phyllosilicates. The results are presented in Table S2 in Supporting Information S1.

3.6. Stable Isotope Compositions

Oxygen and carbon isotope analyses (48 samples) were made in the stable isotope laboratory of the University of Lausanne with a Gas-Bench II interfaced with a Thermo Fisher Scientific DeltaPlus XL isotope ratio mass spectrometer following the method described in Spötl and Vennemann (2003). The stable carbon and oxygen isotope ratios are expressed in delta notation as per mil (‰) relative to the Vienna Pee Dee Belemnite (VPDB) international reference standard. Multiple analyses of an in-house standard (Carrara marble, calibrated to international carbonate standards) were run parallel with the samples to correct raw isotopic values. The analytical precision of the method is better than ±0.1 ‰ (1σ) for both C- and O-isotope compositions. The results are presented in Table S3 in Supporting Information S1.

4. Results

4.1. Log Description

The lower part of the quarry section (Barra Honda Fm.) consists of 64 m of shallow-water limestones with some levels rich in cherts (at −53, −50 and −0.2 m; Figure 4). The upper part of the quarry section is characterized by marls and detrital deposits: The first 7 m above the Barra Honda Fm. are characterized by a high proportion of marls and clays with some cherts, sandy beds, and rare centimetric ash layers (Buenavista Fm.), whereas the uppermost part corresponds to turbiditic deposits with some marl intercalations (Zapotal Mb.). The shorter road section presents the same lithological association as the quarry section, except for the absence of the Zapotal Mb. The first meter of the road section is characterized by massive shallow-water limestones of the Barra Honda Fm.

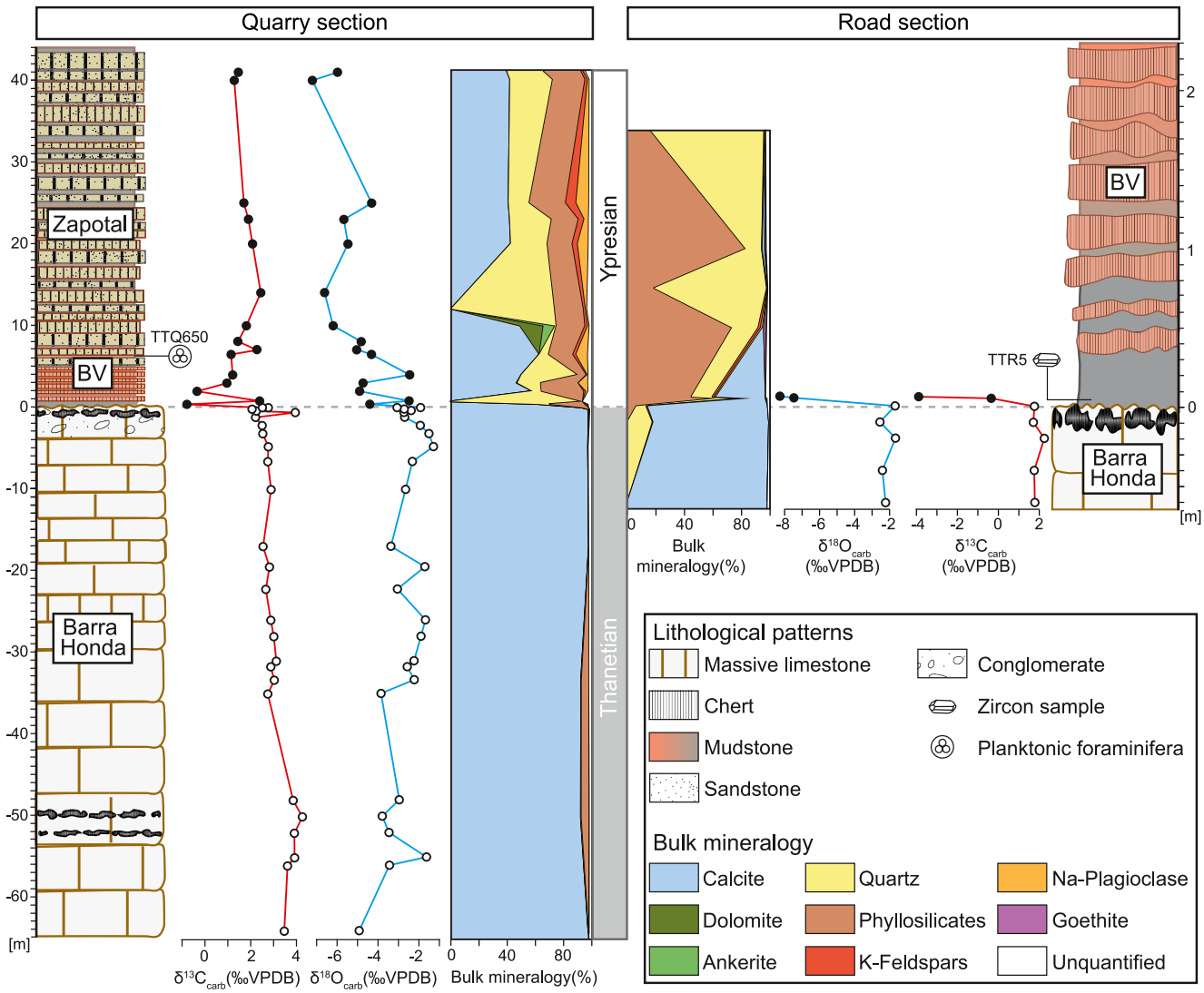

Figure 4. Lithological logs, stable isotope compositions, and bulk rock mineralogy of the quarry and road sections of the upper Barra Honda Formation in the Teresita quarry. BV, Buenavista Formation.

with the presence of cherts a few tens of centimeters below its top. The upper part of the road section (Buenavista Fm.) is dominated by clayey deposits and cherts, with scarce centimetric ash layers (at 0.05, 0.5, and 1 m) and sandy beds.

From a facies perspective, the massive shallow-water limestones of both sections are characterized by red algal packstones and wackestones. Most of these limestones contain *Polystrata alba*, *Melobesia*, larger benthic foraminifera, miliolids, planktonic foraminifera and some siliceous sponges. Pack-to wackestone microfacies and *Polystrata alba* (Denizot, 1968; Pfender, 1936) are very common in most of the layers of the upper Barra Honda Fm. This squamariacean red alga encrusted rhodoids and other firm substrates. It is typical of algal platforms of the Upper Cretaceous and Paleocene, although its range extends from the Barremian to the Eocene (Baumgartner-Mora & Baumgartner, 2016; Massieux & Denizot, 1964; Praturlon, 1966). The upper part of the quarry section (Zapotal Mb.) is characterized by alternating clayey and sandy deposits with low carbonate proportions. Thin sections of the clayey beds show wackestone to mudstone microfacies, including mainly planktonic foraminifera (such as *Morozovella*), sponge spicules, radiolarians, and debris of red algae; sandy beds show higher proportions of feldspars, quartz, amphiboles, and opaque minerals. These deposits are characteristic of an open sea environment receiving a significant detrital input.

4.2. Bulk-Rock Mineralogy

The mineralogy of the quarry and road sections is mainly composed of calcite, quartz, and phyllosilicates, with minor amounts of plagioclase and alkali feldspar, and punctual presence of dolomite, ankerite, and goethite (Figure 4). The unquantified fraction represents generally less than 3 wt% and may correspond to poorly crystallized clays, Fe-oxides, Fe-hydroxides, zeolites and organic matter. For each section, two parts can be distinguished based on the mineralogical contents.

The massive limestones of the Barra Honda Fm. (−65–0 m in the quarry section, −0.7–0 m in the road section) sections consist of 81–98 wt% calcite and very low proportions of quartz and phyllosilicates. The upper part of the quarry and road sections (Buenavista Fm. and Zapotal Mb.) consists of variable proportions of phyllosilicates (0–83 wt%), quartz (1–94 wt%), and calcite (0–63 wt%), which coincide with ash-rich beds, cherts, and clayey deposits (0–44 m in the quarry section, 0–2.3 m in the road section). This mineralogical variability reflects the lithological heterogeneity of the Buenavista Fm. and Zapotal Mb.: (a) Cherts at 0.75 m/12 m in the quarry section and at 0.75 m/1.75 m in the road section present high amounts (>70 wt%) of quartz; (b) ash-rich beds at 0.05 m/0.5 m/1 m in the road section have high proportions (63–83 wt%) of phyllosilicates; (c) marls throughout the quarry section and at one level of the road section show a mix of siliciclastic material (6–30 wt% phyllosilicates, 1 to 40 wt% quartz, 0 to 7.5 wt% alkali feldspar, and 0.5 to 9 wt% plagioclase) and calcite (35–63 wt%).

4.3. Stable Isotope Geochemistry

4.3.1. $\delta^{13}C_{carb}$

$\delta^{13}C_{carb}$ values have a range between −0.8 and 4.3‰ in the quarry section (Figure 4). In the middle to upper Thanetian Barra Honda Fm. (lower part of the section), most values are around 2.8 ‰ except for two positive shifts toward 4.3 ‰ at −50 m and 4.0 ‰ at −0.6 m. A shift of −3.3 ‰ occurs across the boundary between the Barra Honda Fm. and the Buenavista Fm. This is followed by a positive shift to 2.4 ‰ at 0.8 m and a second negative shift to −0.3 ‰ at 2 m, at the base of the lower Ypresian Buenavista Fm. $\delta^{13}C_{carb}$ values increase from −0.3 ‰ at 2 m (Buenavista Fm.) to 2.4 ‰ at 14 m (Zapotal Mb.), after which they steadily decrease toward 1.3 ‰ at 40 m.

$\delta^{13}C_{carb}$ values vary between −3.9 and 2.2 ‰ in the road section. The $\delta^{13}C_{carb}$ values are homogeneous at around 1.8 ‰ in the uppermost Barra Honda Fm. A significant decrease to −3.9 ‰ coincides with the base of the Buenavista Fm. The very low carbonate contents (<2 wt%) of the Buenavista Fm. from 0.5 to 2.3 m precludes the analysis of carbon isotopes.

4.3.2. $\delta^{18}O_{carb}$

$\delta^{18}O_{carb}$ values range from −7.2 to −1.3 ‰ in the quarry section and from −8.3 to −1.7 ‰ in the road section (Figure 4). In both sections, a negative shift occurs around the boundary between the Barra Honda Fm. and the Buenavista Fm., which is 2.5 ‰ in the quarry section and 6.6 ‰ in the road section. In the quarry section, the $\delta^{18}O_{carb}$ record shows an overall decreasing trend above the formational boundary; values decrease from −4.9 ‰ at 2 m to −7.2 ‰ at 40 m, except for two positive excursions toward −2.4 ‰ at 4 m and toward −4.3 ‰ at 25 m.

4.4. Biostratigraphic Ages

Sample TTQ650 is a pelagic limestone rich in planktonic foraminifera (Figure 5) from the Buenavista Fm. that was recovered 6.5 m above the top of the Barra Honda Fm. limestone (quarry section; Figure 4). It yielded *Acarinina* cf. *quetra* (top E3-E6 Zones), *Morozovella subbotinae* (P5-E5 Zones), *Morozovella gracilis* (P5-E5 Zones), *Planorotalites pseudoscitula* (P5-E7 Zones), *Morozovella aequa* (P4c-E5 Zones), *Morozovella* cf. *formosa*, *Morozovella* cf. *lensiformis*, and *Acarinina angulosa* (P5-E7 Zones). The concurrent range of these taxa is from the top E3 to E5 Zones (early to middle Ypresian age), which corresponds to a numerical age of ~54.5–51 Ma (Speijer et al., 2020).

In an earlier study, Bandini et al. (2008) described a radiolarian fauna of sample 01-18-01-02 from the Teresita quarry area in the transition from the Buenavista Fm. to the Zapotal Mb. of the Descartes Fm. The sample was collected about 30 m east of the eastern rim (quarry limits in 2020) of the Teresita quarry at 10° 8′38.29″N and 85°24′49.06″E (Figure 2b). Bandini et al. (2008) concluded a late Thanetian to Ypresian age of this sample. Here,

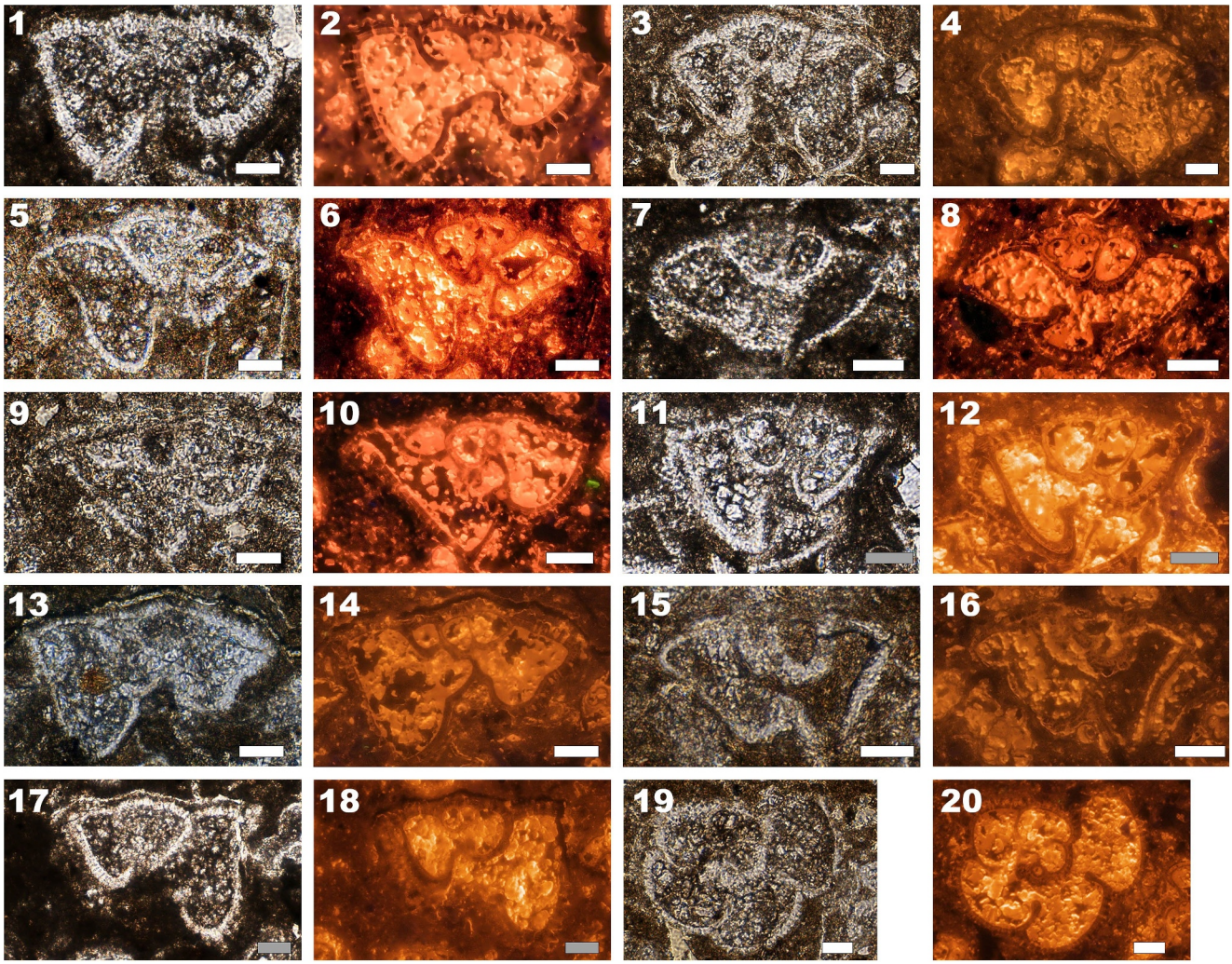

Figure 5. Planktonic foraminifera from the Buenavista Formation (sample TTQ650; quarry section). Transmitted light images: 1, 3, 5, 7, 9, 11, 13, 15, 17, 19. Cathodoluminescence images: 2, 4, 6, 8, 10, 12, 14, 16, 18, 20. White scale bars are 50 µm and gray scale bars are 200 µm (11, 12, 17, 18). 1, 2, *Acarinina* cf. *quetra* (top E3–E6). 3, 4, *Morozovella* cf. *formosa*. 5, 6, *Morozovella gracilis* (P5–E5). 7, 8, *Planorotalites pseudoscitula* (P5–E7). 9–12, *Morozovella subbotinae* (P5–E5). 13–16, *Morozovella aequa* (P4c–E5). 17, 18, *Morozovella* cf. *lensiformis*. 19, 20, *Acarinina angulosa* (P5–E7). The concurrent range of these taxa is from the top E3 to E5 Zones (early to middle Ypresian age).

we slightly revise the taxonomy and the age ranges of the taxa encountered, based on the UA-zonation of Jackett et al. (2008). The sample contains *Lychnocanium carinatum* (UA 11–12), *Podocyrtis* (*Podocyrtis*) *papalis* (UA 11–22), *Phormocyrtis striata exquisite* (UA 3–20), *Stylotrochus nitidus* (UA 5–22), *Circodiscus circularis* (UA 5–22), *Phormocyrtis turgida* (UA 11–22), *Calocyclas hispida* (UA 11–22), *Stylosphaera coronata coronata* (UA 1–22), and *Buryella tetradica* (UA 2–20). Of this association, several species are not older than UAZ 11 (base of the Eocene) and *Lychnocanium carinatum* is restricted to UA 11–12 in Jackett et al. (2008). These two Unitary Associations correlate with the planktonic foraminiferal zones (see Pearson et al., 2006) P5 top half (=E1–E2 Zones) and P6a-b (=E3–E4 Zones), indicating an early Ypresian age. This age overlaps with the age range of planktonic foraminifera from the new sample TTQ650, collectively suggesting that the Buenavista Fm. is restricted to the early to middle Ypresian in the Teresita quarry.

4.5. U–Pb Zircon CA-ID-TIMS Age

Ash-rich layer TTR5 was sampled 5 cm above the limit between massive limestones of the Barra Honda Fm. and overlying clayey beds of the Buenavista Fm (Figure 4). Five single-grain zircons were analyzed from sample TTR5, all of which are concordant within analytical and decay constant uncertainties (Figure 6). Four out of five

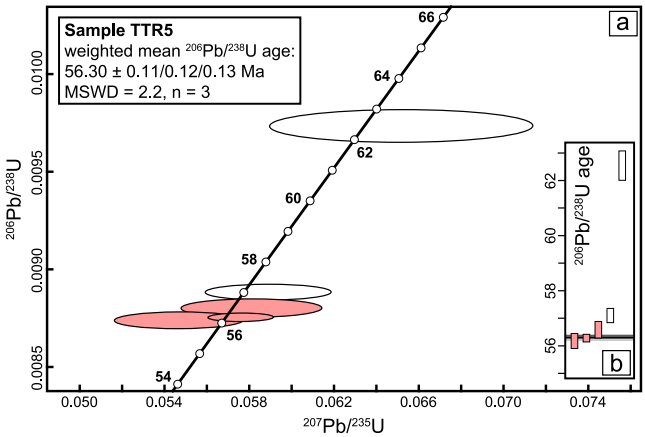

Figure 6. CA-ID-TIMS U–Pb dates for sample TTR5 (lowermost Buenavista Formation; road section). (a) The concordia curve is drawn as a continuous black line. Bold numbers are concordant dates (Ma). Error ellipses are drawn at the 2σ confidence level. Reddish and white error ellipses represent data points included in and excluded from the weighted mean $^{206}Pb/^{238}U$ date calculation, respectively. (b) Ranked single-grain $^{206}Pb/^{238}U$ dates. Box heights representing date uncertainties are drawn at the 2σ confidence level. The horizontal gray band represents the uncertainty of the weighted mean $^{206}Pb/^{238}U$ date calculation (95% confidence).

analyses clustered between 56 and 57 Ma, whereas one analysis yielded a distinctly older age (62.4 Ma) than that of all other analyses. The younger cluster of $^{206}Pb/^{238}U$ dates yielded a weighted mean date of 56.30 Ma ± 0.11/0.12/0.13 Ma (2σ, $n = 3$, MSWD = 2.2), which approximates the depositional age of the ash-rich layer TTR5.

5. Discussion

5.1. Barra Honda–Buenavista Boundary: A Record of the PETM?

The sharp lithological boundary between the Barra Honda and Buenavista formations has been previously interpreted as the demise of the Barra Honda carbonate shoal (Baumgartner-Mora & Baumgartner, 2016). The latter authors argued that the rapid demise of the carbonate shoal occurred through a combination of factors, which are (a) a relative sea level rise due to tectonic subsidence and an eustatic component, (b) and a paleoclimatic change around the Paleocene–Eocene boundary resulting in intensified weathering, river runoff and eutrophication of the forearc basin by detrital input and dissolved organic matter. To discuss how these factors combined to cause the demise of the Barra Honda carbonate shoal, we first use our new data from the Teresita quarry to determine whether the timing of termination of carbonate shoal sedimentation was coeval with the PETM.

A large negative excursion of 3–5 ‰ in $\delta^{13}C_{carb}$ values in both Teresita quarry sections coincides with a prominent decrease in average calcite contents, from 90% calcite in massive limestones of the uppermost Barra Honda Fm. to about 40% calcite in overlying clayey layers of the lowermost Buenavista Fm (Figure 4). Despite having similar carbonate contents ($CaCO_3$ estimated at 28%–39%), the $\delta^{13}C_{carb}$ values at the base of the Buenavista Fm. vary widely (from −0.8 to 2.5 ‰), indicating no correlation between $\delta^{13}C_{carb}$ values and calcium carbonate contents. Instead, the timing of the combined lithological-mineralogical-isotopic change at the Barra Honda–Buenavista boundary is coeval with the PETM, which is supported by new U–Pb zircon CA-ID-TIMS age data as well as new and existing biostratigraphic data. The fact that our new zircon age (56.30 ± 0.13 Ma) of the lowermost Buenavista Fm. is 0.1–0.3 Ma older than the currently established Paleocene–Eocene boundary age (56 Ma) may result from averaging the age of only three zircon grains, among which one older grain (56.5 ± 0.3 Ma) is pooled together with two younger zircon grains (56.2 ± 0.1 and 56.1 ± 0.3 Ma).

The synchronicity of the Barra Honda–Buenavista boundary with the PETM can be further examined by comparing our new $\delta^{13}C_{carb}$ curve of the quarry section to the most recent global $\delta^{13}C$ curve of Speijer et al. (2020). Although the nature and rate of sedimentation differ among the Barra Honda, Buenavista, and Descartes formations, the overall shape of our new $\delta^{13}C_{carb}$ curve of the quarry section approximates the global Thanetian–Ypresian $\delta^{13}C$ curve (Figure 7), with the following key similarities: (a) Two positive carbon isotope excursions occur in the Thanetian; (b) a negative carbon isotope excursion (>2.5‰) characterizes the base of the Ypresian and is related to the PETM; (c) Ypresian $\delta^{13}C$ levels are about 1.5‰ lower after the PETM negative carbon isotope excursion when compared to pre-PETM levels in the Thanetian.

5.2. Growth and Step-Wise Demise of Barra Honda Carbonate Shoal

The onset of shallow-water carbonate sedimentation in the Barra Honda shoal may have been favored by the combination of moderate tectonic subsidence and volcanic quiescence (Figure 8a); for completeness of the model depicted in Figure 8, we present a tectono-stratigraphic model in Appendix A that sets the growth and demise of the Barra Honda carbonate shoal in a broader tectonic context. Tectonic subsidence followed a short-lived episode of km-scale forearc uplift, possibly related to the subduction of bathymetric features (Andjić, Baumgartner, & Baumgartner-Mora, 2018; Figure A1b). Once they entered deeper parts of the subduction interface, the bathymetric features caused cessation of volcanic activity within the Barra Honda area. The proximal forearc basin floor was shortly exposed to subaerial environments before initial moderate subsidence to shallow waters that favored the accumulation of the Barra Honda carbonate shoal (Baumgartner-Mora & Baumgartner, 2016; Jaccard et al., 2001; Figure A1c). Volcanic quiescence resulted in the reduction of the input of proximal coarse-grained

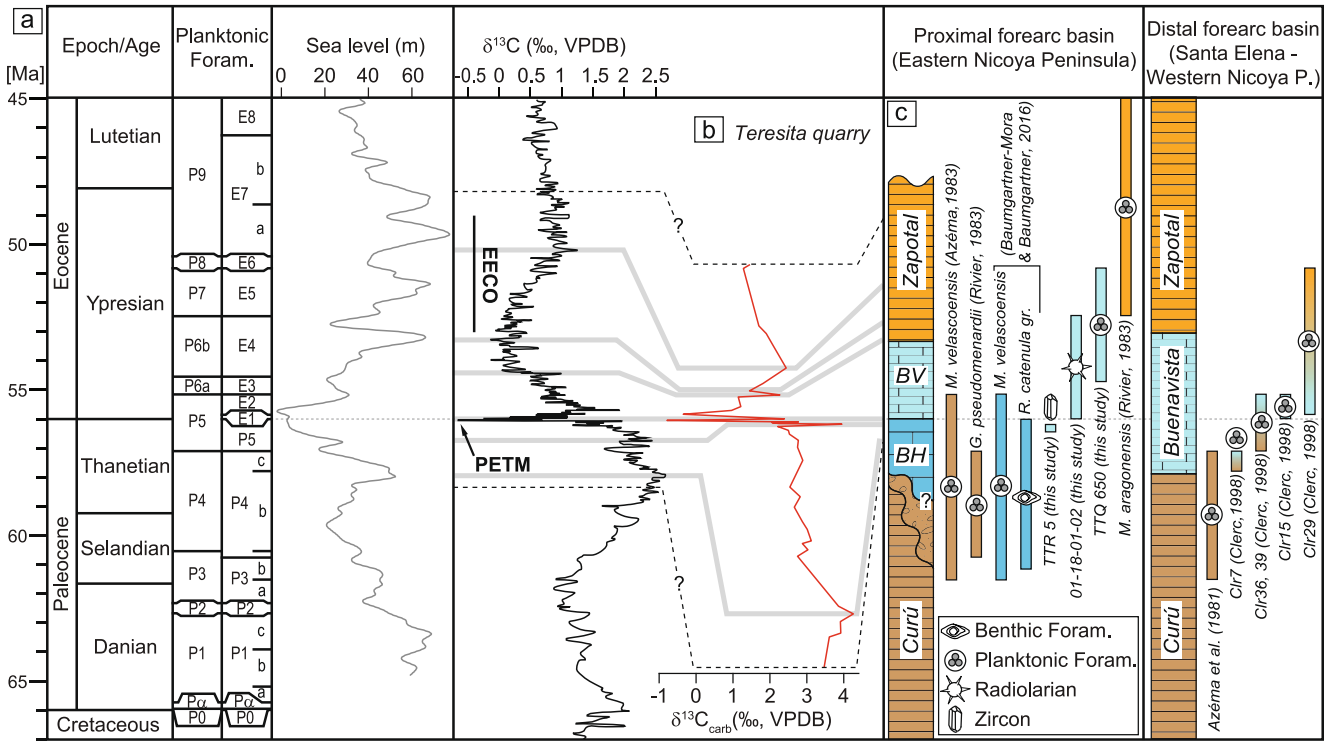

Figure 7. (a) Planktonic foraminifera biozonations (left column: Berggren et al. (1995); right column; Pearson et al. (2006)) and global carbon isotope curve (see Speijer et al., 2020 and references herein) combined with the global mean sea level curve (Miller et al., 2020). Foram, Foraminifera; PETM, Paleocene–Eocene Thermal Maximum; EECO, Early Eocene Climatic Optimum. (b) $\delta^{13}C_{carb}$ curve from the quarry section of the Teresita quarry (this study). The gray lines tentatively correlate the peaks of our new curve with those of the global carbon isotope curve. (c) Simplified chronostratigraphic logs of the Tempisque-Nicoya and northern Santa Elena areas combined with new and previous age constraints. The detailed explanation of previous biostratigraphic constraints is given in Text S1 (Supporting Information S1). BH, upper Barra Honda Formation; BV, Buenavista Formation; P, Peninsula.

volcaniclastic sediments compared with the underlying deep-water forearc formations. Only distal ash particles carried from distant volcanic sources made their way to the upper Barra Honda shoal, as suggested by the discrete contents of phyllosilicates in the massive limestones (Figure 4; Baumgartner-Mora & Baumgartner, 2016). The lifespan of about 5 Ma and the thickness (350 m) of the upper Barra Honda shoal implies an average subsidence rate of the forearc basin of 70 m/Ma during the late Paleocene (61–56 Ma). This subsidence rate is comparable to that of long-lived (>10 Ma) carbonate platforms on passive margins (36–150 m/Ma; Immenhauser, 2022). This, however, raises the question as to why the shallow-water carbonate sedimentation of the upper Barra Honda shoal stopped at the Paleocene–Eocene boundary? In the following sections, we envisage a sequence of events that eventually led to the demise of the upper Barra Honda carbonate shoal during the earliest Ypresian.

5.2.1. Step 1 (56 Ma): Environmental Effects of the PETM

The PETM may have affected the Barra Honda carbonate shoal in at least two ways. Global ocean acidification due to increased CO_2 levels has resulted in reduced rates of accumulation and preservation of carbonate sediments in shelf areas (Bralower et al., 2018). In addition, the rise of sea surface temperatures (about 5°C; e.g., McInerney & Wing, 2011) during the PETM reached levels that were probably beyond the tolerance range of benthic foraminifera, calcareous algae, and CPR of the Barra Honda carbonate shoal (e.g., Scheibner & Speijer, 2008). Moreover, increased precipitation at the onset of the PETM may have caused an increased discharge of terrestrial sedimentary organic matter to shelf areas (e.g., Prieur et al., 2024), favoring the proliferation of non-calcifying organisms such as dinoflagellates and bacteria (Aze et al., 2014; Carmichael et al., 2016; Handley et al., 2012; Kopp et al., 2009; Sluijs et al., 2006). Input of nutrients led to higher surface-water productivity and anoxic to low oxygen levels in bottom shelf waters (Sluijs et al., 2006, 2008). There is currently no quantitative data available from the Tempisque Forearc Basin to constrain whether an absolute increase in the abundance and size of detrital grains occurred during the earliest Eocene. At the outcrop scale, basinal sections of the western Nicoya Peninsula

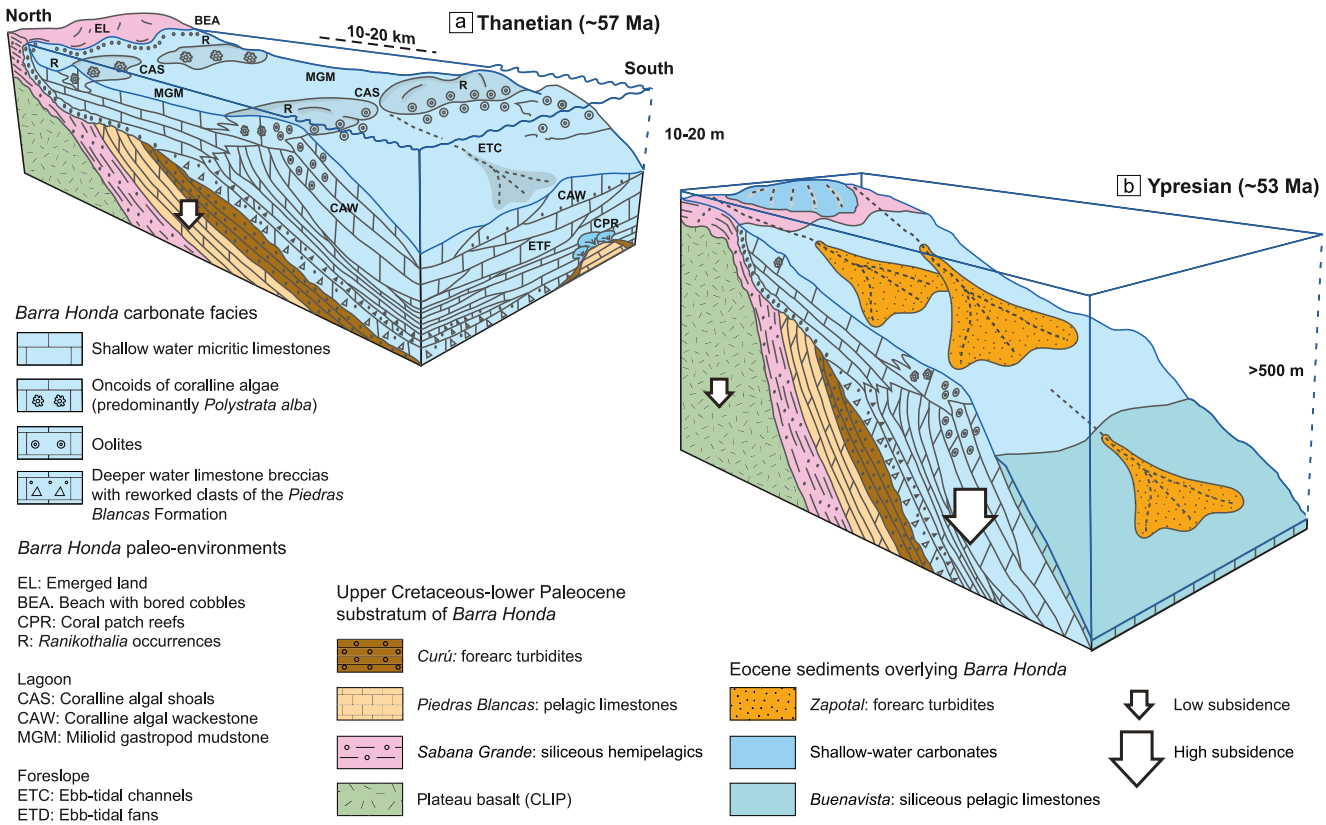

Figure 8. (a) Depositional model of the Barra Honda carbonate shoal during the Thanetian (modified after Baumgartner-Mora & Baumgartner, 2016). Toward the south, Barra Honda limestone breccias encroach on Curú forearc turbidites in an offshore environment and rework lithoclasts from the underlying erosional surface cutting into older formations (Sabana Grande, Piedras Blancas, and Curú). Upsection, massive intraclast breccias give way to platform sediments organized in ebb-tidal fans (ETF). Toward the north, Barra Honda lagoonal micritic facies (MGM) progressively onlap on higher-energy beach and foreshore sediments (BEA) on the eroded structural high during relative sea level rise (i.e., low subsidence). The higher stratigraphic levels of Barra Honda show patchy shoals of coralgal oncoid grain- and packstones (CAS) with *Ranikothalia* sp. (R) and locally oolites. Rare coral patch reefs formed during the Maastrichtian period in the lowermost stratigraphic levels of the Barra Honda Formation. (b) View of the forearc basin 3 Ma after the demise of the Barra Honda carbonate shoal. High forearc subsidence caused deepening of the basin floor to bathyal depths, preventing renewed shallow carbonate production in the Barra Honda carbonate shoal after the Paleocene-Eocene Thermal Maximum (56 Ma). Shallow carbonate deposition may occur only on tectonic highs sheltered from detrital input.

and northern Santa Elena Peninsula (Figure 1b) show that there was no increase in volcanic activity inboard the Nicoya Peninsula around the Paleocene–Eocene boundary: pelagic sedimentation of the Buenavista Fm. dominated that interval (Figure 3) and only airborne ash was brought into the forearc basin from outboard volcanoes (Figure A1d). Rather, the onset of coarse detrital sedimentation of the Zapotal Mb. took place only >1.5 Ma after the demise of the Barra Honda carbonate shoal (Figures 4 and 7), in response to renewed volcanic activity inboard the Nicoya Peninsula (Figures A1e and 8b). Nevertheless, the relative increase of the phyllosilicates/calcite ratio (from 1/18 to 1/2) and feldspars/calcite ratio (from 1/200 to 1/20) in the Teresita quarry is larger than the decrease by 50% of carbonate proportions across the Barra Honda–Buenavista boundary (Figure 4), which may indicate that mud-sized clastic input and turbidity increased on the shelf during the earliest Ypresian (~56 Ma), possibly in response to enhanced river discharge. The resulting reduced light intensity in surface waters would have led to a much shallower photic zone, contributing to the demise of the benthic communities relying on oligotrophic waters. This hypothesis remains to be tested in basinal sections of the Buenavista Fm. (e.g., Santa Elena area; Figures 1b and 3) by establishing whether a change in mineralogical contents coincided with the PETM.

Moreover, the presence of cherts in the Buenavista Fm. suggests an increase in opal production and burial, likely as a response to higher silica input from intensified weathering (e.g., Penman et al., 2019). The latter possibly resulted from enhanced continental weathering and runoff in a warmer climate with increased seasonality of precipitation (Jin et al., 2022; Rush et al., 2021). Excess silica that could not be incorporated in clay-rich layers of the Buenavista Fm. may have precipitated as opal-rich layers that later formed cherts (e.g., Muttoni &

Kent, 2007). The proportion of nutrients brought by upwelling currents versus terrestrial influx remains unconstrainted in this case; climate–carbon cycle models with high-CO_2 levels predict that a weakening of the trade winds would lead to reduced Ekman-induced upwelling and nutrient availability in the equatorial Pacific (Wade et al., 2020; Winguth et al., 2012). However, it remains possible that upwelled water, characterized by low $\delta^{13}C$ values and high nutrient content (e.g., Watanabe et al., 2017), influenced the isotopic compositions of the Buenavista Formation and the production of biogenic silica.

5.2.2. Step 2 (56–55 Ma): Onset of Accelerated Tectonic Subsidence and Eustatic Sea Level Rise

Extreme environmental conditions linked to the PETM were short-lived (about 0.2 Ma; Murphy et al., 2010; Zeebe & Lourens, 2019), after which the production of carbonates resumed in both deep-water and shallow-water settings globally (e.g., Scheibner & Speijer, 2008; Zachos et al., 2005). We speculate that the short duration of the hyperthermal event would have made it possible for the Barra Honda carbonate shoal to recover during the early Ypresian and to resume shallow-water carbonate sedimentation, as suggested by the deposition of early to middle Eocene shallow-water carbonates in the most proximal parts of the forearc basin (Laguna El Jicote; Jaccard et al., 2001; Figures 2a and 3). The fact that this did not occur may be primarily attributable to accelerated forearc subsidence that must have taken place by 55 Ma, not allowing renewed formation and deposition of carbonates in shallow shelf environments (Figure 8b). The fate of uplifted highs in forearc areas affected by subduction of bathymetric features is clear: once the impinging bathymetric feature has been subducted, uplifted forearc areas return to their pre-collisional morphology within 3 Ma at rates similar to those of the uplift episode (e.g., Andjić, Baumgartner, & Baumgartner-Mora, 2018; Corrigan et al., 1990; Cloos, 1993; Meffre & Crawford, 2001; Figure A1). In the case of the Tempisque Forearc Basin, the pre-collisional depth of the forearc basin floor (= Paleocene Curú Fm.) is estimated to be about 3,000 m based on benthic foraminifera (Struss et al., 2008). Assuming that the proximal forearc basin returned to a water depth of 3,000 m within 3 Ma after the PETM, a subsidence rate of 1,000 m/Ma would have brought the Barra Honda shoal to a depth of 1,000 m by 55 Ma, largely exceeding the rate of sediment supply of any carbonate shoal. In contrast, moderate subsidence (70 m/Ma) combined with an early Ypresian 3rd-order eustatic sea level rise (30 m by 55 Ma; Speijer et al., 2020; Figure 7) may not explain the absence of post-PETM recovery of the Barra Honda shoal, because a relative sea level rise of similar magnitude already occurred from 60 to 58 Ma without preventing deposition of shallow-water carbonates.

6. Conclusions

Our work shows a sharp transition from massive shallow-water limestones of the upper Barra Honda Fm. to marl-chert alternations of the Buenavista Fm. in the Tempisque Forearc Basin at the Paleocene–Eocene boundary (56 Ma). The lithological and mineralogical change at the Barra Honda–Buenavista boundary is accompanied by a negative shift in carbon isotope ($\delta^{13}C_{carb}$) values of 3–5 ‰ and an increased detrital input. We postulate that the combination of these two factors caused the demise of the Barra Honda carbonate shoal during the earliest Eocene. First, the PETM led to a significant disturbance of the local oceanographic conditions of the forearc area: during the earliest Ypresian, seawater warming, acidification, eutrophication, and increased river runoff as well as likely upwelling may have led to a shift to siliceous sedimentation in the Buenavista Fm. These environmental changes were highly detrimental to the shallow benthic communities that had formed the upper Barra Honda carbonate shoal during the Thanetian. Second, accelerated subsidence of the Tempisque Forearc Basin closely followed the short-lived PETM event. Shallow shelf areas that were initially favorable to the establishment of the Barra Honda carbonate shoal gave way to deep-water basinal environments by 55 Ma, which did not allow a recovery of the Barra Honda carbonate shoal. After the PETM, the warm climate of the early Eocene was not a limiting factor to the growth of carbonate shoals in Costa Rica and Nicaragua (e.g., Andjić, Baumgartner-Mora, et al., 2018; Baumgartner-Mora & Baumgartner, 2016). Locally, shallow-water carbonate sedimentation occurred on tectonic highs that provided a shelter from river discharges carrying volcaniclastic sediments from active volcanoes.

Appendix A: Margin Response to Rough Crust Subduction

The subduction of bathymetric reliefs influences the structural and magmatic evolution of convergent margins (Cloos, 1993). Whether accretion occurs or not, the primary response of the upper plate is to accommodate the colliding object by kilometric surface uplift in the forearc (Spikings & Simpson, 2014). Hence, the amplitude of

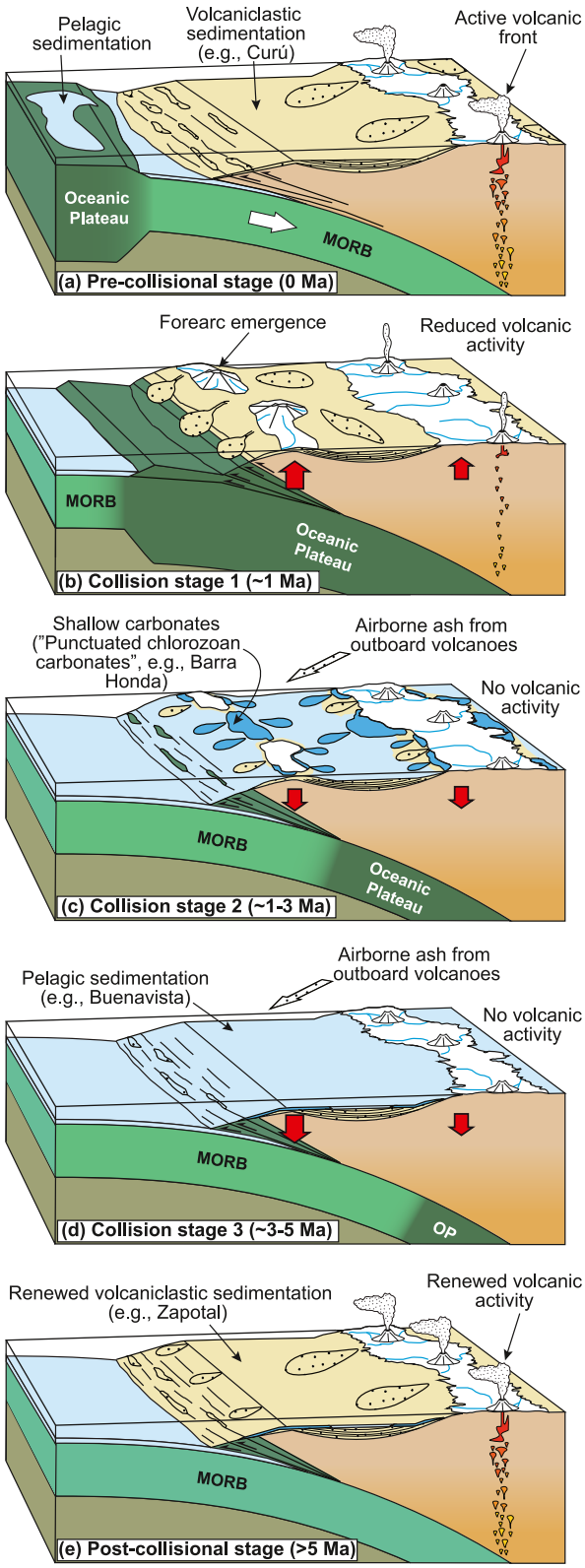

Figure A1.

vertical tectonic motions may be up to two orders of magnitude higher than eustatic variations (Gardner et al., 2013). Short-lived, shallow-water and subaerial environments appear in the inner and/or outer forearc and replace previous long-lived deep-water domains (Dorobek, 2008). Except in the case of stationary subduction of an aseismic ridge or hotspot track (~1,000 km length scale), the duration of forearc uplift is generally shorter than 5 Ma (Meffre & Crawford, 2001; Tetreault & Buiter, 2012; Vogt & Gerya, 2014). Once the colliding bathymetric feature is subducted, the forearc seafloor subsides to its previous water depth; if rough crust subduction causes tectonic erosion of the upper plate, the forearc basin subsides to deeper water depths than in its pre-collisional state (von Huene & Suess, 1988).

A possible secondary response of the upper plate to the collision of bathymetric relief is the cessation of the volcanic activity, which occurs after the initial stage of collision at shallow depths. Spatial gaps in volcanism develop when the leading edge of the object, or its remaining root reaches a greater depth where it may promote flat slab subduction, slab break-off, or modification of dehydration processes in the mantle wedge (Bishop et al., 2017; McGeary et al., 1985; Rosenbaum & Mo, 2011). In the latter case, considering orthogonal convergence rates comprised between ~3.5 and 12 cm/yr (e.g., Young et al., 2019), volcanic arc cessation in response to the arrival of the object at the depth of major slab dehydration and arc magma genesis (~100 km; Ranero et al., 2005) may occur between ~0.8 and 3 Ma after the onset of collision. If the object is long enough (>100 km), a magmatic lull occurs while surface uplift is sustained by the subduction of the object trailing edge.

The identification of arc gaps in ancient volcanic formations is uncertain, because igneous rocks are often discontinuously preserved. Drawing mainly on examples from Central America, Andjić, Baumgartner, and Baumgartner-Mora (2018) have recently shown that forearc sedimentary rocks can record lulls in the magmatic history of arcs (Figure A1). In particular, the abrupt interruption of volcaniclastic sedimentation in forearc basins and its replacement by pelagic sedimentation indicate a demise in the production of arc-derived material. After the collision of the bathymetric relief, renewed

Figure A1. Formation and demise of carbonate shoals in response to rough crust subduction and arc extinction. The model is based on plateau collision events discussed in Baumgartner-Mora and Baumgartner (2016) and Andjić et al. (2016, 2018a, 2018b, 2019a). The drawing style is after Frisch et al. (2011). (a) Subduction of normal oceanic crust (labeled as MORB–Mid-oceanic ridge basalt) leads to arc volcanic activity. (b) Subduction of the bathymetric feature causes surface uplift in the forearc and progressive cessation of volcanic activity as the leading edge of the bathymetric feature reaches the window of major slab dehydration. The input of eroded detrital material and ongoing surface uplift hamper the formation and preservation of shallow-water carbonates. (c) Low forearc subsidence due to renewed subduction of normal oceanic crust at shallow depth. Ongoing subduction of the trailing edge of the bathymetric feature in the window of major slab dehydration sustains volcanic quiescence. The subsidence of the forearc and the reduced volcaniclastic input allow the short-lived development of shallow-water carbonate shoals (e.g., Barra Honda Fm.). (d) High forearc subsidence leads to the drowning of shallow-water carbonate factories and return to deep-water pre-collisional levels. Due to its ongoing subduction in the window of major slab dehydration, the trailing edge of the bathymetric feature sustains volcanic quiescence. (e) Subduction of normal oceanic crust in the window of major slab dehydration leads to renewed volcanic arc activity, which results in deep-water volcaniclastic sedimentation. Small-sized shallow-water carbonate factories may be established in areas sheltered from the detrital input derived from active volcanoes.

subduction of normal oceanic crust in the window of major fluid release and related volcanic activity resumed the supply of detrital material to the forearc basin. Interestingly, Andjić, Baumgartner, and Baumgartner-Mora (2018) have identified delays between the onset/end of forearc uplift and onset/end of volcanic activity in past collision episodes of oceanic plateau in Costa Rica (e.g., late Paleocene). Here, shallow-water carbonates (i.e., late Paleocene Barra Honda Fm.; Figure 1b) deposited in response to forearc uplift formed earlier than pelagic sedimentation (i.e., Buenavista Fm.) resulting from the cessation of volcanic arc activity; this may be the consequence of the colliding object interacting first with shallow levels of the upper plate before being subducted to greater depths and modifying dehydration processes in the mantle wedge (Figure A1a). In contrast, the demise of shallow-water carbonate factories intervened earlier than the termination of pelagic sedimentation; this may result from the tail of the colliding object interacting with the mantle wedge later than it was the case with the shallow upper plate (Figure A1d).

Data Availability Statement

New data generated in this study are available in the Supporting Information S1, and can also be found in https://doi.org/10.5281/zenodo.15268142.

Acknowledgments
We are thankful to the previous owner of the Santa Teresita quarry for allowing us the access to the outcrops. We thank Benita Putlitz for the help with zircon extraction. This work was supported by the Swiss National Science Foundation Grant 185067 to C.B.M. We are thankful to Marine Prieur and an anonymous reviewer for their thoughtful reviews.

References

Adatte, T., Stinnesbeck, W., & Keller, G. (1996). Lithostratigraphic and mineralogic correlations of near K/T boundary clastic sediments in Northeastern Mexico: Implications for origin and nature of deposition. *Geological Society of America Special Paper*, *307*, 211–226. https://doi.org/10.1130/0-8137-2307-8.211

Aguilar, T., & Denyer, P. (2001). Una nueva especie de Euphylia (Scleractinia: Caryophylliidae) en las calizas de Barra Honda (Paleógeno), Costa Rica. *Revista de Biologia Tropical*, *2*, 195–201.

Andjić, G., Baumgartner, P. O., & Baumgartner-Mora, C. (2018). Rapid vertical motions and formation of volcanic arc gaps: Plateau collision recorded in the forearc geological evolution (Costa Rica margin). *Basin Research*, *30*(5), 863–894. https://doi.org/10.1111/bre.12284

Andjić, G., Baumgartner, P. O., & Baumgartner-Mora, C. (2019a). Collision of the Caribbean large igneous province with the Americas: Earliest evidence from the Forearc of Costa Rica. *The Geological Society of America Bulletin*, *131*(9-10), 1555–1580. https://doi.org/10.1130/B35037.1

Andjić, G., Baumgartner-Mora, C., & Baumgartner, P. O. (2016). An upper Paleogene shallowing-upward sequence in the southern Sandino Forearc Basin (NW Costa Rica): Response to tectonic uplift. *Facies*, *62*(2), 1–35. https://doi.org/10.1007/s10347-016-0463-y

Andjić, G., Baumgartner-Mora, C., Baumgartner, P. O., & Petrizzo, M. R. (2018). Tectono-stratigraphic response of the Sandino Forearc Basin (N-Costa Rica and W-Nicaragua) to episodes of rough crust and oblique subduction. *The Depositional Record*, *4*(1), 90–132. https://doi.org/10.1002/dep2.40

Andjić, G., Escuder-Viruete, J., Baumgartner-Mora, C., Baumgartner, P. O., Mitchell, S. F., Caron, M., & Caus, E. (2019). Sedimentary record of arc-continent collision along Mesozoic SW North America (Siuna Belt, Nicaragua). *Tectonics*, *38*(12), 4399–4425. https://doi.org/10.1029/2019TC005741

Aubry, M. P., Ouda, K., Dupuis, C., Berggren, W. A., & Van Couvering, J. A., & Boundary TMOTWGOTP. (2007). The Global Standard Stratotype-Section and Point (GSSP) for the base of the Eocene series in the Dababiya section (Egypt). *Episodes*, *30*(4), 271–286. https://doi.org/10.18814/epiiugs/2007/v30i4/003

Aze, T., Pearson, P. N., Dickson, A. J., Badger, M. P. S., Bown, P. R., Pancost, R. D., et al. (2014). Extreme warming of tropical waters during the Paleocene-Eocene thermal maximum. *Geology*, *42*(9), 739–742. https://doi.org/10.1130/G35637.1

Babila, T. L., Penman, D. E., Hönisch, B., Kelly, D. C., Bralower, T. J., Rosenthal, Y., & Zachos, J. C. (2018). Capturing the global signature of surface ocean acidification during the Palaeocene-Eocene Thermal Maximum. *Philosophical Transactions of the Royal Society A: Mathematical, Physical and Engineering Sciences*, *376*, 2017072. https://doi.org/10.1098/rsta.2017.0072

Bandini, A. N., Flores, K., Baumgartner, P. O., Jackett, S.-J., & Denyer, P. (2008). Late cretaceous and paleogene radiolaria from the Nicoya Peninsula, Costa Rica: A tectonostratigraphic application. *Stratigraphy*, *5*(1), 3–21. https://doi.org/10.29041/strat.05.1.02

Baumgartner, P. O., Flores, K., Bandini, A. N., Girault, F., & Cruz, D. (2008). Upper Triassic to cretaceous radiolaria from Nicaragua and Northern Costa Rica—The Mesquito composite oceanic terrane. *Ofioliti*, *33*, 1–19. https://doi.org/10.4454/ofioliti.v33i1.356

Baumgartner, P. O., Mora, C. R., Butterlin, J., Sigal, J., Glacon, G., Azéma, J., & Bourgois, J. (1984). Sedimentación y paleogeografía del Cretácico y Cenozoico del litoral pacifico de Costa Rica. *Revista Geologica de America Central*, *1*, 57–136. https://doi.org/10.15517/rgac.v0i01.10469

Baumgartner-Mora, C., & Baumgartner, P. O. (2016). Paleocene-earliest Eocene larger benthic foraminifera and Ranikothalia-bearing carbonate Paleo-environments of Costa Rica (South Central America). *Micropaleontology*, *62*(6), 453–508. https://doi.org/10.47894/mpal.62.6.04

Baumgartner-Mora, C., Baumgartner, P. O., & Andjic, G. (2019). *A new model: Punctuated Chlorozoan Carbonates-biotic response to accretion tectonics and volcanism (Cretaceous-Cenozoic, Mid-America)*. 34th IAS Meeting of Sedimentology.

Berggren, W. A., Kent, D. V., Swisher, C. C., III, & Aubry, M.-P. (1995). A revised Cenozoic geochronology and chronostratigraphy. In W. A. Berggren, D. V. Kent, M.-P. Aubry, & J. Hardenbol (Eds.), *Geochronology, time scales and global stratigraphic correlation. A unified temporal framework for a historical geology* (Vol. 54, pp. 129–212). SEPM Special Publication. https://doi.org/10.2110/pec.95.04.0129

Bishop, B. T., Beck, S. L., Zandt, G., Wagner, L., Long, M., Antonijevic, S. K., et al. (2017). Causes and consequences of flat-slab subduction in Southern Peru. *Geosphere*, *13*(5), 1392–1407. https://doi.org/10.1130/GES01440.1

Bornemann, A., Norris, R. D., Lyman, J. A., D'haenens, S., Groeneveld, J., Röhl, U., et al. (2014). Persistent environmental change after the Paleocene–Eocene thermal maximum in the Eastern North Atlantic. *Earth and Planetary Science Letters*, *394*, 70–81. https://doi.org/10.1016/j.epsl.2014.03.017

Bosence, D., (2005). A genetic classification of carbonate platforms based on their basinal and tectonic settings in the Cenozoic. *Sedimentary Geology*, *175*(1–4), 49–72. https://doi.org/10.1016/j.sedgeo.2004.12.030

Bowring, J. F., McLean, N. M., & Bowring, S. A. (2012). Engineering cyber infrastructure for U-Pb geochronology: Tripoli and U-Pb-Redux. *Geochemistry, Geophysics, Geosystems*, *12*(6). https://doi.org/10.1029/2010GC003479

Bralower, T. J., Kump, L. R., Self-Trail, J. M., Robinson, M. M., Lyons, S., Babila, T., et al. (2018). Evidence for shelf acidification during the onset of the Paleocene-Eocene thermal maximum. *Paleoceanography and Paleoclimatology*, *33*(12), 1408–1426. https://doi.org/10.1029/2018PA003382

Calvo, C., & Bolz, A. (1991). La Formación Espíritu Santo (Costa Rica): Sistema de plataforma carbonatada autóctona del Paleoceno superior-Eoceno inferior. *Revista Geologica de America Central*, *13*, 91–95. https://doi.org/10.15517/rgac.v0i13.13079

Carmichael, M. J., Lunt, D. J., Huber, M., Heinemann, M., Kiehl, J., LeGrande, A., et al. (2016). A model–model and data–model comparison for the early Eocene hydrological cycle. *Climate of the Past*, *12*(2), 455–481. https://doi.org/10.5194/cp-12-455-2016

Chesnel, V., López-Murillo, E., Löser, H., & Velázquez Heras, J. E. (2024). Puerto Níspero, a Maastrichtian carbonate platform in Costa Rica. *Journal of South American Earth Sciences*, *141*, 104953. https://doi.org/10.1016/j.jsames.2024.104953

Cloos, M. (1993). Lithospheric buoyancy and collisional orogenesis: Subduction of oceanic Plateaus, continental margins, island arcs, spreading ridges, and seamounts. *The Geological Society of America Bulletin*, *105*(6), 715–737. https://doi.org/10.1130/0016-7606(1993)105<0715:LBACOS>2.3.CO;2

Colosimo, A. B., Bralower, T. J., & Zachos, J. C. (2006). Evidence for lysocline shoaling at the Paleocene/Eocene thermal maximum on Shatsky rise, Northwest Pacific. In T. J. Bralower, I. Premoli Silva, & M. J. Malone (Eds.), *Proceedings of the ocean drilling program, scientific results* (Vol. 198, pp. 1–36). https://doi.org/10.2973/odp.proc.sr.198.112.2006

Condon, D. J., Schoene, B., McLean, N. M., Bowring, S. A., & Parrish, R. (2015). Metrology and traceability of U–Pb isotope dilution geochronology (EARTHTIME Tracer Calibration Part I). *Geochimica et Cosmochimica Acta*, *164*, 464–480. https://doi.org/10.1016/j.gca.2015.05.026

Corrigan, J., Mann, P., & Ingle, J. C. (1990). Forearc response to subduction of the Cocos ridge, Panama-Costa Rica. *The Geological Society of America Bulletin*, *102*(5), 628–652. https://doi.org/10.1130/0016-7606(1990)102<0628:FRTSOT>2.3.CO;2

Dengo, G. (1962). *Estudio Geológico de la Región de Guanacaste* (p. 112). Instituto Geografico Nacional.

Denizot, M. (1968). *Les Algues Floridées Encroutantes (à l'exclusion des Corallinacées). Laboratoire de Cryptogamie* (p. 310). Musée National d'Histoire Naturelle de Paris.

Denyer, P., Aguilar, T., & Montero, W. (2014a). Cartografia geológica de la Peninsula de Nicoya, Costa Rica: Estratigrafia y tectónica: San José, Costa Rica, Editorial Universidad de Costa Rica (p. 207).

Denyer, P., Aguilar, T., & Montero, W. (2014b). Cartografia geológica de la Peninsula de Nicoya, Costa Rica: Mapas geológicos: San José, Costa Rica, Editorial Universidad de Costa Rica, scale 1:50,000, 21 sheets.

Denyer, P., & Alvarado, G. E. (2007). *Mapa Geológico de Costa Rica 1:400'000*. Librería Francesa S.A.

Dickens, G. R., Castillo, M. M., & Walker, J. C. G. (1997). A blast of gas in the latest Paleocene: Simulating first-order effects of massive dissociation of oceanic methane hydrate. *Geology*, *25*(3), 259–262. https://doi.org/10.1130/0091-7613(1997)025<0259:ABOGIT>2.3.CO;2

Di Marco, G., Baumgartner, P. O., & Chanell, J. E. T. (1995). Late Cretaceous-Early Tertiary paleomagnetic data and a revised tectonostratigraphic subdivision of Costa Rica and western Panama. In P. Mann (Ed.), *Geologic and tectonic development of the Caribbean Plate boundary in southern Central America* (Vol. 295, pp. 1–27). Geological Society of America Special Papers. https://doi.org/10.1130/SPE295-p1

Dorobek, S. L. (2008). Carbonate-platform facies in volcanic-arc settings: Characteristics and controls on deposition and stratigraphic development. In A. E. Draut, P. D. Clift, & D. W. Scholl (Eds.), *Formation and applications of the sedimentary record in arc collision zones* (Vol. 463, pp. 55–90). Geological Society of America Special Papers. https://doi.org/10.1130/2008.2436(04

Egger, H., Heilmann-Clausen, C., & Schmitz, B. (2000). The Paleocene/Eocene-boundary interval of a Tethyan deep-sea section (Austria) and its correlation with the North Sea basin. *Bulletin de la Societe Geologique de France*, *171*(2), 207–216. https://doi.org/10.2113/171.2.207

Escalona, A., Norton, I. O., Lawver, L. A., & Gahagan, L. (2021). Quantitative Plate tectonic reconstructions of the Caribbean Region from Jurassic to present. In C. Bartolini (Ed.), *South America-Caribbean-Central Atlantic plate boundary* (Vol. 123, pp. 239–263). American Association of Petroleum Geologists Memoir. https://doi.org/10.1306/13692247M1233849

Escuder-Viruete, J., Baumgartner, P. O., & Castillo-Carrión, M. (2015). Compositional diversity in ophiolitic peridotites as result of a multi-process history: The Santa Elena ophiolite, northwest Costa Rica. *Lithos*, *231*, 16–34. https://doi.org/10.1016/j.lithos.2015.05.019

Flores, K. (2006). *Jurassic–Late Cretaceous oceanic crustal terranes and arc-derived sediments south Chortis Block (NE Nicaragua to NW Costa Rica). Preliminary results of two key areas: Nicoya Peninsula and Siuna District. D.E.A. thesis* (p. 107). University of Lausanne.

Flores, K. (2009). *Mesozoic oceanic terranes of southern Central America: Geology, geochemistry and geodynamics*. [Ph.D. thesis] (p. 290). University of Lausanne.

Flores, K., Denyer, P., & Aguilar, T. (2003a). Nueva propuesta estratigráfica: Geología de las hojas Matambú y Talolinga, Guanacaste, Costa Rica. *Revista Geologica de America Central*, *28*, 131–138. https://doi.org/10.15517/rgac.v0i28.7793

Flores, K., Denyer, P., & Aguilar, T. (2003b). Nueva propuesta estratigráfica: Geología de la hoja Abangares, Guanacaste, Costa Rica. *Revista Geologica de America Central*, *29*, 127–136. https://doi.org/10.15517/rgac.v0i29.7780

Frisch, W., Meschede, M., & Blakey, R. (2011). Subduction zones, island arcs and active continental margins. In W. Frisch, M. Meschede, & R. Blakey (Eds.), *Plate tectonics* (pp. 91–122). Springer. https://doi.org/10.1007/978-3-540-76504-2_7

Gardner, T. W., Fisher, D. M., Morell, K. D., & Cupper, M. L. (2013). Upper-plate deformation in response to flat slab subduction inboard of the aseismic Cocos Ridge, Osa Peninsula, Costa Rica. *Lithosphere*, *5*(3), 247–264. https://doi.org/10.1130/L251.1

Gerstenberger, H., & Haase, G. (1997). A highly effective emitter substance for mass spectrometric Pb isotope ratio determinations. *Chemical Geology*, *136*(3–4), 309–312. https://doi.org/10.1016/S0009-2541(96)00033-2

Gibbs, S. J., Stoll, H. M., Bown, P. R., & Bralower, T. J. (2010). Ocean acidification and surface water carbonate production across the Paleocene-Eocene Thermal Maximum. *Earth and Planetary Science Letters*, *295*(3–4), 583–592. https://doi.org/10.1016/j.epsl.2010.04.044

Giusberti, L., Rio, D., Agnini, C., Backman, J., Fornaciari, E., Tateo, F., & Oddone, M. (2007). Mode and tempo of the Paleocene-Eocene thermal maximum in an expanded section from the Venetian pre-Alps. *The Geological Society of America Bulletin*, *119*(3–4), 391–412. https://doi.org/10.1130/B25994.1

Gradstein, F. M. (2020). *Chapter 3 evolution and biostratigraphy* (pp. 74–87). Elsevier B.V. https://doi.org/10.1016/B978-0-12-824360-2.00003-6

Handley, L., O'Halloran, A., Pearson, P. N., Hawkins, E., Nicholas, C. J., Schouten, S., et al. (2012). Changes in the hydrological cycle in tropical East Africa during the Paleocene Eocene thermal maximum. *Palaeogeography, Palaeoclimatology, Palaeoecology*, *329*, 10–21. https://doi.org/10.1016/j.palaeo.2012.02.002

Hiess, J., Condon, D. J., McLean, N., & Noble, S. R. (2012). 238U/235U systematics in terrestrial uranium-bearing minerals. *Science*, *335*(6076), 1610–1614. https://doi.org/10.1126/science.1215507

Huber, B. T., Petrizzo, M. R., Young, J. R., Falzoni, F., Gilardoni, S. E., Bown, P. R., & Wade, B. S. (2016). Pforams@mikrotax: A new online taxonomic database for planktonic foraminifera. *Micropaleontology*, *62*(6), 429–438. https://doi.org/10.47894/mpal.62.6.02

Immenhauser, A. (2022). On the delimitation of the carbonate burial realm. *The Depositional Record*, *8*(2), 524–574. https://doi.org/10.1002/dep2.173

Jaccard, S., & Münster, M. (2001). *Etude géologique multidisciplinaire de la plateforme de Barra Honda (Guanacaste, Costa Rica): Sédimentologie, isotopes stables du strontium, du carbone, de l'Oxygène et contexte géodynamique*. [D.E.A. thesis] (p. 98). Université de Lausanne.

Jaccard, S., Münster, M., Baumgartner, P. O., Baumgartner-Mora, C., & Denyer, P. (2001). Barra Honda (upper Paleocene-lower Eocene) and El Viejo (Campanian- Maastrichtian) carbonate platforms in the Tempisque area (Guanacaste, Costa Rica). *Revista Geologica de America Central*, *24*, 9–28. https://doi.org/10.15517/rgac.v0i24.8550

Jackett, S.-J., Baumgartner, P. O., & Bandini, A. N. (2008). A new low-latitude late Paleocene-early Eocene radiolarian biozonation based on unitary associations: Applications for accreted terranes. *Stratigraphy*, *5*(1), 39–62. https://doi.org/10.29041/strat.05.1.04

Jin, S., Kemp, D. B., Jolley, D. W., Vieira, M., Zachos, J. C., Huang, C., et al. (2022). Large-scale, astronomically paced sediment input to the north Sea Basin during the Paleocene Eocene thermal maximum. *Earth and Planetary Science Letters*, *579*, 117340. https://doi.org/10.1016/j.epsl.2021.117340

Kemp, D. B., & Sadler, P. M. (2014). Climatic and Eustatic signals in a global compilation of shallow marine carbonate accumulation rates. *Sedimentology*, *61*(5), 1286–1297. https://doi.org/10.1111/sed.12112

Klug, H. P., & Alexander, L. E. (1974). *X-ray diffraction procedures: For polycrystalline and amorphous materials* (p. 992). John Wiley and Sons.

Kopp, R. E., Schumann, D., Raub, T. D., Powars, D. S., Godfrey, L. V., Swanson-Hysell, N. L., et al. (2009). An Appalachian amazon? Magnetofossil evidence for the development of a tropical river-like system in the mid- Atlantic United States during the Paleocene-Eocene thermal maximum. *Paleoceanography*, *24*(4), 1–17. https://doi.org/10.1029/2009PA001783

Kübler, B. (1983). Dosage quantitatif des minéraux majeurs des roches sédimentaires par diffraction X. Cahier de l'institut de Géologie de Neuchâtel. *Série*, *AX*(1.1–1.2), 1–13.

Ludwig, K. R. (1991). ISOPLOT for MS-DOS, a plotting and regression program for radiogenic isotope data, for IBM-PC compatible computers, version 2.75. *U.S. Geological Survey, Open-File Report*, *91–445*, 45. https://doi.org/10.3133/ofr91445

Lyle, M., Wilson, P. A., & Janecek, T. R. (2002). Leg 199 summary. *Proceedings of the Ocean Drilling Program - Initial Reports* (Vol. 199, 1–87). https://doi.org/10.2973/odp.proc.ir.199.101.2002

Massieux, M., & Denizot, M. (1964). Rapprochement du genre Pseudolithothamnium Pfender avec le genre actuel Ethelia Weber Van Bosse (Algues Florideae, Squamariaceae). *Revue de Micropaleontologie*, *7*, 31–42.

McGeary, S., Nur, A., & Benavraham, Z. (1985). Spatial gaps in arc volcanism: The effect of collision or subduction of oceanic plateaus. *Tectonophysics*, *119*(1–4), 195–221. https://doi.org/10.1016/0040-1951(85)90039-3

McInerney, F. A., & Wing, S. L. (2011). The Paleocene-Eocene thermal maximum: A perturbation of carbon cycle, climate, and biosphere with implications for the future. *Annual Review of Earth and Planetary Sciences*, *39*(1), 489–516. https://doi.org/10.1146/annurev-earth-040610-133431

McLean, N. M., Bowring, J. F., & Bowring, S. A. (2011). An algorithm for U-Pb isotope dilution data reduction and uncertainty propagation. *Geochemistry, Geophysics, Geosystems*, *12*(6), Q0AA18. https://doi.org/10.1029/2010GC003478

McLean, N. M., Condon, D. J., Schoene, B., & Bowring, S. A. (2015). Evaluating uncertainties in the calibration of isotopic reference materials and multi-element isotopic tracers (EARTHTIME Tracer Calibration Part II). *Geochimica et Cosmochimica Acta*, *164*, 481–501. https://doi.org/10.1016/j.gca.2015.02.040

Meffre, S., & Crawford, A. J. (2001). Collision tectonics in the New Hebrides arc (Vanuatu). *Island Arc*, *10*(1), 33–50. https://doi.org/10.1046/j.1440-1738.2001.00292.x

Miller, K. G., Browning, J. V., Schmelz, W. J., Kopp, R. E., Mountain, G. S., & Wright, J. D. (2020). Cenozoic sea-level and cryospheric evolution from deep-sea geochemical and continental margin records. *Science Advances*, *6*(20), eaaz1346. https://doi.org/10.1126/sciadv.aaz1346

Mora, C., & Baumgartner, P. O. (1985). *Mapa geológico del sur de la Península de Nicoya. Escala 1:50 000*. Instituto Geografico Nacional Rica.

Mora, S. (1981). Barra Honda. Editorial universidad estatal a distancia. *Serie Educación Ambiental*, *5*, 115.

Murphy, B. H., Farley, K. A., & Zachos, J. C. (2010). An extraterrestrial He-3-based timescale for the Paleocene-Eocene thermal Maximum (PETM) from Walvis ridge, IODP site 1266. *Geochimica et Cosmochimica Acta*, *74*(17), 5098–5108. https://doi.org/10.1016/j.gca.2010.03.039

Murphy, M. A., & Salvador, A. (1999). International stratigraphic guide–an abridged edition. *Episodes*, *22*(4), 255–271. https://doi.org/10.18814/epiiugs/1999/v22i4/002

Muttoni, G., & Kent, D. V. (2007). Widespread formation of cherts during the early Eocene climate optimum. *Palaeogeography, Palaeoclimatology, Palaeoecology*, *253*(3–4), 348–362. https://doi.org/10.1016/j.palaeo.2007.06.008

Olsson, R. K., Hemleben, C., Berggren, W. A., & Huber, B. T. (1999). Atlas of Paleocene planktonic foraminifera. *Smithsonian Contributions to Paleobiology*, *85*, 252. https://doi.org/10.5479/si.00810266.85.1

Pearson, P. N., Olsson, R. K., Huber, B. T., Hemleben, C., & Berggren, W. A. (2006). *Atlas of Eocene planktonic foraminifera* (Vol. 41, p. 514). Cushman Foundation Special Publication.

Penman, D. E. (2016). Silicate weathering and north Atlantic silica burial during the Paleocene-Eocene thermal maximum. *Geology*, *44*(9), 731–734. https://doi.org/10.1130/G37704.1

Penman, D. E., Honisch, B., Zeebe, R. E., Thomas, E., & Zachos, J. C. (2014). Rapid and sustained surface ocean acidification during the Paleocene-Eocene Thermal Maximum. *Paleoceanography*, *29*(5), 357–369. https://doi.org/10.1002/2014PA002621

Penman, D. E., Keller, A., D'haenens, S., Kirtland Turner, S., & Hull, P. M. (2019). Atlantic deep-sea cherts associated with Eocene hyperthermal events. *Paleoceanography and Paleoclimatology*, *34*, 287–299. https://doi.org/10.1029/2018PA0035)03

Petrizzo, M. R., Wade, B. S., & Gradstein, F. M. (2020). Planktonic foraminifera. In F. M. Gradstein, J. G. Ogg, M. D. Schmitz, & G. M. Ogg (Eds.), *Geologic time scale*. https://doi.org/10.1016/C2020-1-02369-3.1390.

Pfender, J. (1936). Sur un organisme constructeur des calcaires crétacés et nummulitiques, Pseudolithothamnium album, n. g. nov. sp. *Bulletin de la Societe Geologique de France*, *6*, 303–308.

Praturlon, A. (1966). Algal assemblages from Lias to Paleocene in southern Latium-Abruzzi: A review. *Bollettino della Societa Geologica Italiana*, *85*, 167–194.

Prieur, M., Whittaker, A. C., Nuriel, P., Jaimes-Gutierrez, R., Garzanti, E., Roigé, M., et al. (2024). Fingerprinting enhanced floodplain reworking during the Paleocene-Eocene Thermal Maximum in the southern Pyrenees (Spain): Implications for channel dynamics and carbon burial. *Geology*, *52*(9), 651–655. https://doi.org/10.1130/G52180.1

Ranero, C. R., Villasenor, A., Phipps Morgan, J., & Weinrebe, W. (2005). Relationship between bend-faulting at trenches and intermediate-depth seismicity. *Geochemistry, Geophysics, Geosystems*, *6*(12), Q12002. https://doi.org/10.1029/2005GC000997

Rivier, F. (1983). *Síntesis geológica y mapa geológico del area del Bajo Tempisque Guanacaste, Costa Rica* (pp. 7–30). Instituto Geografico Nacional, Informe semestral, Costa Rica.

Romito, S., & Mann, P. (2020). *Tectonic terranes underlying the present-day Caribbean plate: Their tectonic origin, sedimentary thickness, subsidence histories, and regional controls on hydrocarbon resources* (Vol. 504, pp. 343–377). Geological Society, London, Special Publications. https://doi.org/10.1144/SP504-2019-221

Rosenbaum, G., & Mo, W. (2011). Tectonic responses to the subduction of high bathymetric relief. *Gondwana Research*, *19*(3), 571–582. https://doi.org/10.1016/j.gr.2010.10.007

Rush, W. D., Kiehl, J. T., Shields, C. A., & Zachos, J. C. (2021). Increased frequency of extreme precipitation events in the North Atlantic during the PETM: Observations and theory. *Palaeogeography, Palaeoclimatology, Palaeoecology*, *568*, 110289. https://doi.org/10.1016/j.palaeo.2021.110289

Sanchez, J., Mann, P., Carvajal-Arenas, L. C., & Bernal-Olaya, R. (2019). Regional transect across the western Caribbean Sea based on integration of geologic, seismic reflection, gravity, and magnetic data. *Bulletin of the American Association of Petroleum Geologists*, *103*(2), 303–343. https://doi.org/10.1306/05111816516

Schaltegger, U., Ovtcharova, M., Gaynor, S. P., Schoene, B., Wotzlaw, J.-F., Davies, J. F., et al. (2021). Long-term repeatability and interlaboratory reproducibility of high-precision ID-TIMS U–Pb geochronology. *Journal of Analytical Atomic Spectrometry*, *36*(7), 1466–1477. https://doi.org/10.1039/D1JA00116G

Scheibner, C., & Speijer, R. P. (2008). Late Paleocene–early Eocene Tethyan carbonate platform evolution–A response to long-and short-term Paleoclimatic change. *Earth-Science Reviews*, *90*(3–4), 71–102. https://doi.org/10.1016/j.earscirev.2008.07.002

Schmitz, B., Pujalte, V., & Nunez-Betelu, K. (2001). Climate and sea-level perturbations during the initial Eocene thermal maximum: Evidence from siliciclastic units in the Basque basin (Ermua, Zumaia and Trabakua Pass), northern Spain. *Palaeogeography, Palaeoclimatology, Palaeoecology*, *165*(3–4), 299–320. https://doi.org/10.1016/S0031-0182(00)00167-X

Schmitz, M. D., & Schoene, B. (2007). Derivation of isotope ratios, errors, and error correlations for U-Pb geochronology using 205Pb-235U-(233U)-spiked isotope dilution thermal ionization mass spectrometric data. *Geochemistry, Geophysics, Geosystems*, *8*. https://doi.org/10.1029/2006GC001492

Schoene, B., Crowley, J. L., Condon, D. J., Schmitz, M. D., & Bowring, S. A. (2006). Reassessing the uranium decay constants for geochronology using ID-TIMS U-Pb data. *Geochimica et Cosmochimica Acta*, *70*(2), 426–445. https://doi.org/10.1016/j.gca.2005.09.007

Sluijs, A., Brinkhuis, H., Crouch, E. M., John, C. M., Handley, L., Munsterman, D., et al. (2008). Eustatic variations during the Paleocene-Eocene greenhouse world. *Paleoceanography*, *23*(4), PA4216. https://doi.org/10.1029/2008PA001615

Sluijs, A., Schouten, S., Pagani, M., Woltering, M., Brinkhuis, H., Damsté, J. S. P., et al. (2006). Subtropical Arctic Ocean temperatures during the Palaeocene/Eocene thermal maximum. *Nature*, *441*(7093), 610–613. https://doi.org/10.1038/nature04668

Speijer, R. P., Pälike, H., Hollis, C. J., Hooker, J. J., & Ogg, J. G. (2020). The Paleogene period. In F. M. Gradstein, J. G. Ogg, M. D. Schmitz, & G. M. Ogg (Eds.), *Geologic time scale 2020* (pp. 1087–1140). Elsevier. https://doi.org/10.1016/B978-0-12-824360-2.00028-0

Spikings, R., & Simpson, G. (2014). Rock uplift and exhumation of continental margins by the collision, accretion, and subduction of buoyant and topographically prominent oceanic crust. *Tectonics*, *33*(5), 635–655. https://doi.org/10.1002/2013TC003425

Spötl, C., & Vennemann, T. W. (2003). Continuous-flow IRMS analysis of carbonate minerals. *Rapid Communications in Mass Spectrometry*, *17*(9), 1004–1006. https://doi.org/10.1002/rcm.1010

Struss, I., Artiles, V., Cramer, B., & Winsemann, J. (2008). The petroleum system in the Sandino Forearc Basin, offshore western Nicaragua. *Journal of Petroleum Geology*, *31*(3), 221–244. https://doi.org/10.1111/j.1747-5457.2008.00418.x

Taylor, F. W., Mann, P., Bevis, M. G., Edwards, R. L., Cheng, H., Cutler, K. B., et al. (2005). Rapid forearc uplift and subsidence caused by impinging bathymetric features: Examples from the New Hebrides and Solomon arcs. *Tectonics*, *24*(6), TC6005. https://doi.org/10.1029/2004tc001650

Tetreault, J. L., & Buiter, S. (2012). Geodynamic models of terrane accretion: Testing the fate of island arcs, oceanic plateaus, and continental fragments in subduction zones. *Journal of Geophysical Research*, *117*(B8), B08403. https://doi.org/10.1029/2012JB009316

Vogt, K., & Gerya, T. V. (2014). From oceanic plateaus to allochthonous terranes: Numerical modelling. *Gondwana Research*, *25*(2), 494–508. https://doi.org/10.1016/j.gr.2012.11.002

von Huene, R., & Suess, E. (1988). Ocean drilling program Leg 112, Peru continental margin: Part 1, tectonic history. *Geology*, *16*(10), 934–938. https://doi.org/10.1130/0091-7613(1988)016<0934:ODPLPC>2.3.CO;2

Wade, B. S., O'Neill, J. F., Phujareanchaiwon, C., Ali, I., Lyle, M., & Witkowski, J. (2020). Evolution of deep-sea sediments across the Paleocene-Eocene and Eocene-Oligocene boundaries. *Earth-Science Reviews*, *211*, 103403. https://doi.org/10.1016/j.earscirev.2020.103403

Wade, B. S., Pearson, P. N., Berggren, W. A., & Pälike, H. (2011). Review and revision of Cenozoic tropical planktonic foraminiferal biostratigraphy and calibration to the geomagnetic polarity and astronomical time scale. *Earth-Science Reviews*, *104*(1–3), 111–142. https://doi.org/10.1016/j.earscirev.2010.09.003

Watanabe, T. K., Watanabe, T., Yamazaki, A., Pfeiffer, M., Garbe-Schönberg, D., & Claereboudt, M. R. (2017). Past summer upwelling events in the Gulf of Oman derived from a coral geochemical record. *Scientific Reports*, *7*(1), 4568. https://doi.org/10.1038/s41598-017-04865-5

Weber, P. (2013). *Assessing sedimentary evolution by means of Sr-isotope ratios: 3 case studies on the Caribbean Plate (Cretaceous: Nicoya Peninsula, Costa Rica, Tertiary: Hess rise, and La Désirade, Guadeloupe, France)*. [Ph.D. thesis] (p. 176). University of Lausanne.

Wilson, M. E. J., & Lokier, S. W. (2002). Siliciclastic and volcaniclastic influences on equatorial carbonates: Insights from the Neogene of Indonesia. *Sedimentology*, *49*(3), 583–601. https://doi.org/10.1046/j.1365-3091.2002.00463.x

Winguth, A. M., Thomas, E., & Winguth, C. (2012). Global decline in ocean ventilation, oxygenation, and productivity during the Paleocene-Eocene thermal maximum: Implications for the benthic extinction. *Geology*, *40*(3), 263–266. https://doi.org/10.1130/G32529.1

Young, A., Flament, N., Maloney, K., Williams, S., Matthews, K., Zahirovic, S., & Müller, R. D. (2019). Global kinematics of tectonic plates and subduction zones since the late Paleozoic Era. *Geoscience Frontiers*, *10*(3), 989–1013. https://doi.org/10.1016/j.gsf.2018.05.011

Zachos, J. C., Kroon, D., Blum, P., et al. (2004). In *Proceedings of the ocean drilling Program, Scientific results, initial reports* (Vol. 208). Ocean Drilling Program. https://doi.org/10.2973/odp.proc.ir.208.2004

Zachos, J. C., Rohl, U., Schellenberg, S. A., Sluijs, A., Hodell, D. A., Kelly, D. C., et al. (2005). Rapid acidification of the ocean during the Paleocene-Eocene thermal maximum. *Science*, *308*(5728), 1611–1615. https://doi.org/10.1126/science.1109004

Zeebe, R. E., & Lourens, L. J. (2019). Solar System chaos and the Paleocene–Eocene boundary age constrained by geology and astronomy. *Science*, *365*(6456), 926–929. https://doi.org/10.1126/science.aax0612

Zeebe, R. E., & Zachos, J. C. (2007). Reversed deep-sea carbonate ion basin gradient during Paleocene-Eocene Thermal Maximum. *Paleoceanography*, *22*(3), PA3201. https://doi.org/10.1029/2006PA001395

References From the Supporting Information

Arenillas, I., Molina, E., & Schmitz, B. (1999). Planktic foraminiferal and ∂13C isotopic changes across the Paleocene/Eocene boundary at Possagno (Italy). *International Journal of Earth Sciences*, *88*(2), 352–364. https://doi.org/10.1007/s005310050270

Astorga, A. (1987). *El Cretácico Superior y el Paleógeno de la vertiente pacífica de Nicaragua meridional y Costa Rica septentrional: Origen, evolución y dinámica de las cuencas profundas relacionadas al margen convergente de Centroamérica. Tesis de Licenciatura* (p. 250). Universidad de Costa Rica.

Astorga, A. (1988). Geodinámica de las cuencas del Cretácico Superior- Paleógeno de la región "forearc" del Sur de Nicaragua y Norte de Costa Rica. *Revista Geologica de America Central*, *9*, 1–40. https://doi.org/10.15517/rgac.v0i09.12959

Azéma, J., Glaçon, G., & Tournon, J. (1981). Nouvelles données sur le Paléocène à Foraminifères planctoniques de la bordure Pacifique du Costa Rica. *Compte Rendu Sommaire des Seances de la Societe Geologique de France*, *3*, 85–88.

Clerc, C. (1998). Foraminifères planctoniques en sections de la couverture du terrain de Nicoya (Costa Rica). Crétacé supérieur- Paléogène. Travail de diplôme, Université de Genève (p. 121).

Denyer, P. (2019). Perspectiva geológica del noroeste de Costa Rica: Historia, evolución y cartografía. *San José, Costa Rica. Editorial Universidad de Costa Rica*.

Jiang, M.-J., & Robinson, E. (1987). Calcareous nannofossils and larger Foraminifera in Jamaican rocks of Cretaceous to early Eocene age. In R. Ahmad (Ed.), *Proceedings of a workshop on the status of Jamaican geology* (pp. 24–51). Geological Society of Jamaica, Signart Printing House, Kingston, Jamaica.

Kelly, D. C., Bralower, T. J., Zachos, J. C., Premoli Silva, I., & Thomas, E. (1996). Rapid diversification of planktonic foraminifera in the tropical Pacific (ODP Site 865) during the late Paleocene thermal maximum. *Geology*, *24*(5), 423–426. https://doi.org/10.1130/0091-7613(1996)024<0423:RDOPFI>2.3.CO;2

Lundberg, N. (1982). Evolution of the slope landward of the Middle America Trench, Nicoya Peninsula, Costa Rica. In *Geological society, London, special publications*, J. K. Leggett (Ed.) Geological Society, London, Special Publications (Vol. 10(1), 131–147). https://doi.org/10.1144/GSL.SP.1982.010.01.9

Miller, K. G., Kominz, M. A., Browning, J. V., Wright, J. D., Mountain, G. S., Katz, M. E., et al. (2005). The phanerozoic record of global sealevel change. *Science*, *310*(5752), 1293–1298. https://doi.org/10.1126/science.1116412

Molina, E., Arenillas, I., & Pardo, A. (1999). High resolution planktic foraminiferal biostratigraphy and correlation across the Paleocene/Eocene boundary in the Tethys. *Bulletin de la Societe Geologique de France*, *170*, 521–530.

Pak, D. K., & Miller, K. G. (1992). Paleocene to Eocene benthic foraminiferal isotopes and assemblages: Implications for deepwater circulation. *Paleoceanography*, *7*(4), 405–422. https://doi.org/10.1029/92PA01234

Patino, L. C., Alvarado-Induni, G. E., & Vogel, T. A. (2004). Early arc magmatism: Geochemical characteristics of volcanic clasts from Punta Sámara, Costa Rica. *Revista Geologica de America Central*, *30*, 117–125. https://doi.org/10.15517/rgac.v0i30.7279

Robinson, E., & Wright, R. M. (1993). Jamaican Paleogene larger foraminifera. In R. M. Wright & E. Robinson (Eds.), *Biostratigraphy of Jamaica* (Vol. 182, pp. 283–345). Geological Society of America Memoir. https://doi.org/10.1130/MEM182-p283

Sprechmann, P. (1982). Estratigrafia de Costa Rica I: Unidades estratigraficas sedimentarias. *5th Latinamerican Geological Congress, Argentina*.

Sprechmann, P. (1984). Manual de geologia de Costa Rica: Estratigrafia. 320 p. Editorial Universidad de Costa Rica.

Weyl, R. (1980). *Geology of Central America* (p. 371). Gebrüder Borntraeger.

Zoppis Bracci, L., & Del Giudice, D. (1958). Geología de la costa del Pacifico de Nicaragua. *Boletín del Servicio Geológico Nacional de Nicaragua*, *2*, 19–68.